

# Bayesian Calibration for Activity Based Models

Laura Schultz, Joshua Auld and Vadim Sokolov\*

First Draft: December, 2019  
This Draft September 3, 2022

## Abstract

We consider the problem of calibration and uncertainty analysis for activity-based transportation simulators. Activity-Based Models (ABMs) rely on statistical modeling of individual travelers' behavior to predict higher-order travel patterns in metropolitan areas. Input parameters are typically estimated from traveler surveys using maximum likelihood. We develop an approach that uses a Gaussian Process emulator to calibrate those parameters using traffic flow data. Our approach extends traditional emulators to handle the high-dimensional and non-stationary nature of transportation simulators. We introduce a deep learning dimensionality reduction model that is jointly estimated with Gaussian Process model to approximate the simulator. We demonstrate the methodology using several simulated examples as well as by calibrating key parameters of the Bloomington, Illinois model.

## 1 Introduction

Transportation activity-based simulators (ABMs) represent an individual traveler's activity patterns and trips throughout the day by using nested choice models. The generated trips are then simulated in a traffic flow simulator to learn system-level patterns. These behaviorally-realistic models require a high-resolution representation of network flows and, thus, are computationally expensive. The very same flexibility which makes these simulation models appealing, also makes their calibration problems intractable, with the number of simulations required to find an optimal solution growing exponentially as the input dimension increases [90, 70]. As a result, the use of these simulators is currently limited to what-if analysis.

This paper focuses on calibrating the static choice model parameters used in activity-based simulators. The goal of calibration is to find values of the simulator's input parameters  $\theta$  that minimizes the deviance between observed data and simulator's outputs. We assume that observed  $y(z)$  and the simulated  $\eta(z, \theta)$  traffic flows are related via the following equation:

$$y(z) = \eta(z, \theta) + \epsilon(\theta) + e, \quad (1)$$

where  $z$  is a set of observed inputs the modeler is certain about (e.g. day of the week) and  $\theta$  is a set uncertain inputs (e.g. value of traveler's time) that need to be calibrated;  $\epsilon(\theta)$  captures any structural inadequacy of the simulator; and  $e$  represents the observation error and residual variation inherent to the true process which generates  $y$ .

The problem of simulator calibration is well studied in the transportation literature [7]. However, research has primarily focused on traditional, aggregated models, which use origin-destination estimation to represent demand [18, 108, 107]. The typical approach has been to use optimization methods [106, 105]; specifically, by using simulation-based optimization approaches which treat the simulator as a black-box [97, 67, 8, 110], such as Genetic Algorithm (GA) [21, 62, 66], Simultaneous Perturbation Stochastic Approximation (SPSA) [61, 23, 57], and exhaustive evaluation [45], with relative success [104]. However, due to the non-linear, non-stationary, and stochastic nature of new ABM simulators, straightforward application of existing optimization techniques have limited applicability given they require large number of simulation runs [34].

---

\*Vadim Sokolov is Assistant Professor in Operations Research at George Mason University. email:vsokolov@gmu.edu

Some alternatives substitute a complex simulator with a set of lower-fidelity simulators to approximate the ABM’s solution [22, 75] or through hierarchical decomposition to more manageable sub-problems [16, 68, 8]. However, while these multi-fidelity approaches do improve on the problem of costly run times, the number of samples required still remains high and the curse of dimensionality prevents us from using these methods in high-dimensional problems. For example, if a 20-dimensional simulator’s run could be reduced to one second, it would still take 3.171 trillion years of computing ( $10^{20}$  runs) to evaluate solutions on a grid with just 10 points per dimension. Further, additional development of these lower-fidelity models would be necessary and results in significantly increased modeling efforts and resources, e.g. modeler’s effort and budgets. Divide-and-conquer methods, or parallelization-based techniques, have also been studied to address the dimensional issue [40, 106, 102, 25, 29, 89, 100] but can only provide a multiplicative expansion to an exponential growth in sampling requirements.

Another set of techniques relies on Bayesian updating to solve the calibration problem [46, 36, 35, 109]. A probabilistic surrogate function is automatically constructed to emulate the simulation’s behavior without the additional modelling development of previous methods. The integration of available data allows the non-parametric estimate to recommend optimal samples sequentially [42, 95, 28, 77, 79], which makes the approach sample-efficient [15, 38, 75, 42, 48, 98, 93, 94, 80]. We propose to use this Bayesian surrogate-based approach to automatically construct a low-fidelity surrogate to solve the calibration problem. We use a non-parametric Gaussian Process (GP) as our surrogate [82] and expand the calibration framework proposed by [53, 87, 88].

However, in order to apply the algorithm to our transportation simulators, two drawbacks of the GP surrogate must be addressed. First, it assumes that the underlying function to be approximated is smooth [91, 31], which our ABMs are not. Some approaches which assume a specific functional form of the simulator were proposed to tackle the non-smooth nature of the problem [42, 86, 13, 85] but require prior knowledge to choose the right form. Second, while capable of reproducing a wide range of behaviors and providing a highly flexible fit [44], the non-parametric nature of GPs also hinders success in high-dimensional settings without large sample sizes. As a result, GP modeling, uncertainty analysis, and optimization applications have historically been restricted to characteristically low-dimensional problems [92, 24, 10, 14, 54, 96, 99]; the curse of dimensionality problem continues to be unsolved [91]. We address both of those drawbacks by introducing a deep learning pre-processing step that reduces dimensionality and changes the nature of the simulator function.

Previously proposed dimensionality reduction techniques make specific assumptions, e.g. that simulator function is additive and exploit this structure [33, 32, 52, 63, 71, 12, 24, 6]. Dimensionality Reduction seeks influential substructures to obtain a low dimensional input that is a projection of the original high-dimensional one. Dimensionality Reduction techniques [72, 2, 41] include variable screening [64, 20, 83, 73], kernel construction [59, 26, 101, 32, 49], Partial Least Squares (PLS), Principal Component Analysis (PCA), and sliced inverse regression (SIR) [30].

In essence, our contribution lies in developing a surrogate model that combines the non-linear deterministic dimensionality reduction technique with the probabilistic GP model and developing an inference scheme that jointly estimates parameters of those two components. We then apply the sequential design experiment techniques along with the proposed surrogate model to implement Bayesian optimization for an activity-based transportation simulator. We show that our proposed surrogate outperforms ordinary GPs and more complex GPs which are designed to deal with non-stationary data.

The rest of the paper is organized as follows: in Section 2, we detail the typical structure of transportation simulators and the paper’s example ABM POLARIS [3]; Section 3.1 provides exploratory analysis of the simulator to motivate our methodology. Section 3 outlines the methodological contribution of this paper; Section 4 demonstrates our methodology on the problem of calibrating our example model; and Section 5 discusses avenues for future research.

## 2 POLARIS: an Agent-Based Model

An activity-based transportation simulator has two components: network and demand. The demand simulator includes several inputs, such as land-use variables, socio-demographic characteristics of the population, road infrastructure, and congestion patterns. Then the activity-based models generate the trip tables.

Parameters of statistical models that generate the trips are typically estimated using small-sample surveys. Inadequacy of the models combined with low sample sizes lead to structural errors and large unexplained variance in those models. The network component uses trips generated by the demand model as an input and calculates the resulting congestion patterns. Figure 1 shows an example of the overall architecture.

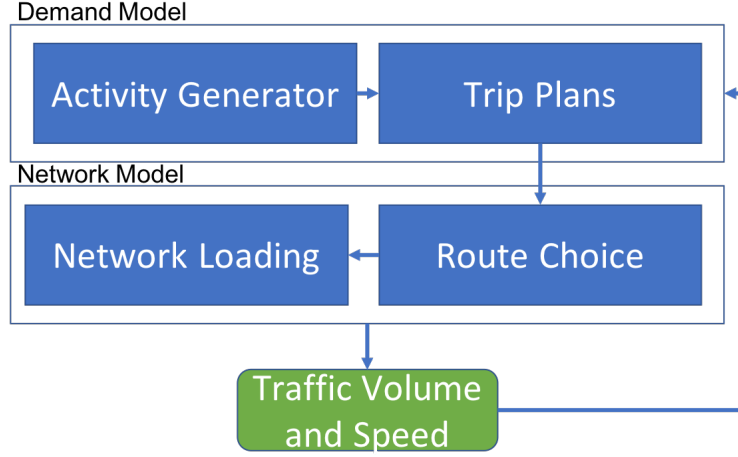


Figure 1: An example of simulation flow diagram for an integrated transportation simulator

Typically, the demand-network models are executed several times in a loop to achieve an approximation to equilibrium in the network flows. The traffic volume and speed are the main outputs of the simulator that are used in our calibration procedure by comparing with the measured traffic flows.

## 2.1 Demand Module

A demand module first generates a set of trips for each of the travelers (agents) by first assigning a destination and series of choices to individual users. For POLARIS, a Weibull hazard model is used [4] to estimate the probability  $h_{ij}(t)$  of an activity of type  $j$  occurring for traveler  $i$  at time  $t$ :

$$h_{ij}(t) = \gamma_j t^{\gamma_j - 1} \exp(-\beta_j^T x_i), \quad (2)$$

where  $\gamma_j$  is the shape parameter of the Weibull distribution,  $x_i$  are observed attributes of the traveler and  $\beta$  are the model parameters estimated from a survey.

Next, the order and timing for each activity, such as location, start time, duration and mode, is allocated by the trip planning model which is a set of discrete choice models; POLARIS uses the multinomial logit model [11] to choose the destinations for each given activity type. This model is derived from random utility maximization theory, which states that for each decision maker  $n$  and location  $i$ , there is a utility  $U_{in}$  associated with selecting location  $i$ . A generalized linear model for utility is assumed

$$U_{in} = \beta^T x_{ni} + \epsilon_{in}, \quad (3)$$

where  $\beta_i$  represent the parameters estimated from survey data;  $x_{ni}$  are observed attributes of traveler  $n$  and location  $i$ , such as travel time to, and land use attributes of,  $i$ ; and  $\epsilon_{in}$  is an unobservable random error which follows a Gumbel distribution so that the probability of traveler  $n$  choosing destination  $i$  is given by

$$p_{ni} = \frac{\exp(V_{in})}{\sum_{j \in C_n} \exp(V_{jn})}. \quad (4)$$

Here  $V_{in} = \beta^T x_{ni}$ . The choice set  $C_n$  is formed using a space-time prism constraint [3].

Once attributed, the planning order is determined using the Ordered Probit model, which is an extension of the basic probit model for binary responses extended to ordinal responses  $y \in \{1, \dots, K\}$ . Under this model, the probability of  $y$  being equal to  $k$  is given by

$$p(y = k) = p(l \leq \alpha_k) - p(l \leq \alpha_{k-1}),$$

where  $\alpha_1, \dots, \alpha_{K-1}$  is a set of threshold-values, and  $l = \beta^T x + \epsilon$ ,  $\epsilon \sim N(0, \Sigma)$ .

## 2.2 Network Module

Once the trips, defined by the origin, destination, departure time and mode, are generated, the network model performs Dijkstra’s algorithm to determine route on the transportation network. Once these choices on routes are selected, destination and departure times are assigned to each agent and the resulting congestion levels within the road network is produced. Kinematic Wave theory of traffic flow [74] is used to simulate traffic flow on each road segment. This model has been recognized as an efficient and effective method for large-scale networks [60] and dynamic traffic assignment formulations.

In particular, the Lighthill-Whitham-Richards (LWR) model [58, 78] along with discretization scheme proposed by Newell [74] is used. The LWR model is a macroscopic traffic flow model. It is a combination of a conservation law defined via a partial differential equation and a fundamental diagram. The fundamental diagram is a flow-density relation  $q(x, t) = q(\rho(x, t))$ . The nonlinear first-order partial differential equation describes the aggregate behavior of drivers. The density  $\rho(x, t)$  and flow  $q(x, t)$ , which are continuous scalar functions, satisfy the equation

$$\frac{\partial \rho(x, t)}{\partial t} + \frac{\partial q(x, t)}{\partial x} = 0.$$

This equation is solved numerically by discretizing time and space.

In addition, intersection operations are simulated for signal controls, as well as stop and yield signs. The input for LWR model is a fundamental diagram that relates flow and density of traffic flow on a road segment. The key parameter of fundamental diagram is critical flow, which is also called road capacity. The capacity is measured in number of vehicles per hour per lane, and provides theoretical maximum of flow that can be accommodated by a road segment.

## 3 Bayesian Model Formulation

Our calibration problem is formulated as an optimisation problem with the objective of minimizing the difference between the observed traffic flows  $y$  and simulated flows  $\eta(z, \theta)$ :

$$\theta^* \in \arg \min_{\theta \in A} \mathcal{L}(y, \eta(z, \theta)) \quad (5)$$

where the vector of input parameters  $\theta \in \mathbb{R}^p$  represent coefficients of choice models used by the transportation ABMs and the constraint set  $A \in \mathbb{R}^{p \times 2}$  represents a modeler’s prior knowledge about feasible ranges of the parameters  $a_{i1} \leq \theta_i \leq a_{i2}$ . The univariate loss function  $\mathcal{L}$  calculates how close the observed data  $y$  is to the simulated outputs  $\eta(z, \theta)$ . Without loss of generality, we omit the static variable  $z$  that is known to the modeler and does not need to be calibrated.

The form of the loss function  $\mathcal{L}$  depends on the observation error  $e$ , and systematic error  $\epsilon(\theta)$  terms of Equation 1. Assuming both of the error terms to be Normal with zero mean, we get the least-squares loss function

$$\mathcal{L}(y, \eta(\theta)) = \|y - \eta(\theta)\|_2^2$$

For brevity, we will refer to the loss function as  $\mathcal{L}(\theta)$  going forward.

Because our application involves an ABM simulator  $\eta$  which is computationally expensive and has only a limited number of simulations which can be carried out, we use the Bayesian Optimisation (BO) approach for model calibration.

We start by assuming that the loss function is continuous and placing a prior over continuous functions defined on  $[0, \infty]$ . Then, we compute an ensemble of initial simulator runs at  $N$  input setting  $\{\theta^{(i)}, \mathcal{L}(\theta^{(i)})\}_{i=1}^N$ .

These values  $[\theta^{(1)}, \dots, \theta^{(N)}]$  are generated using Latin hypercube sampling [65]. With the set of input-output pairs, a Bayesian statistical model is formulated and integrate with the data to calculate its posterior. Each additional sample recommended for evaluation is then iteratively chosen using the sequential design of experiment paradigm; the loss function is evaluated according to a chosen heuristic to determine the optimal next sample which has the greatest potential for improving the estimated solution [69].

We use a Gaussian Process (GP) to model the value of the loss function  $\mathcal{L}(\theta)$  at new locations and to perform the sequential design of experiment. One key component of our formulation is the use of dimensionality reduction pre-processing to accelerate the search for optimal location. More specifically, we use deep learning, non-linear dimension reducer. In this section we describe the dimensionality reduction and Bayesian optimisation techniques we propose to solve the problem of calibrating a high-dimensional transportation simulator.

### 3.1 Exploratory Analysis of POLARIS Simulator Runs

We use  $d = 5$  input parameters  $\theta = [\theta_1, \dots, \theta_5]$ , described in Table 1, in order to demonstrate our framework. These parameters were identified by one of the model developers as the most important set to be calibrated.

Component	Name	Description	Range
Mode Choice	HBO_B_male_taxi	Effect of traveler's sex on taxi utility	[0.298, 2.298]
Mode Choice	NHB_B_dens_bike	Effect of population density on bike utility	[6.601, 8.601]
Mode Choice	HBO_ASC_TAXI	Intercept in taxi utility	[2.34, 4.34]
Destination Choice	THETAR_WORK	Effect of retail accessibility	[-8.553, -6.553]
Destination Choice	GAMMA_SERVICE	Distance decay	[7.038, 9.038]

Table 1: Activity-Based model parameters and their lower and upper bounds

For each input parameter setting, sum of simulated turn delays, averaged over 5-minute intervals for the 24 hours period are taken as the simulator outputs. The resulting 288 outputs are used to calculate the mean squared error objective function  $\mathcal{L}(\theta)$  between simulated and observed values:

$$\mathcal{L}(\theta) = \frac{1}{288} \sum_{i=1}^{288} (y_i - \eta(\theta)_i)^2. \quad (6)$$

To explore the nature of the input-output relationships, we use the Morris screening technique [84], which is widely used for high-dimensional models, to explore potential non-linearity and any interactions among the input parameters  $\theta$ . The Morris procedure starts by generating an initial set of origin samples  $\theta^{(1)}, \dots, \theta^{(r)}$ . Each variable in  $\theta^{(i)}$  is uniformly sampled from its corresponding range. A set of  $r$  trajectories are then built, where each trajectory starts at point  $\theta^{(i)}$  and is generated by perturbing each of the  $d$  variables one at a time by a fixed value  $\delta$ . For our analysis, we use  $r = 6$  trajectories constructed by  $d = 5$  steps, thus resulting in a sample of  $N = 36$  input-output pairs.

Given this initial sample set, we calculate the finite difference, called the Elementary Effect (EE), for each trajectory  $i$  and each variable  $j$ :

$$EE_{i,j} = \frac{\mathcal{L}(\theta_1^i, \theta_2^i, \dots, \theta_j^i + \delta, \dots, \theta_d^i) - \mathcal{L}(\theta_1^i, \theta_2^i, \dots, \theta_j^i, \dots, \theta_m^i)}{\delta} \quad (7)$$

Then Morris procedure analyses elementary effects using three statistics

$$\mu_j = \frac{1}{r} \sum_{i=1}^r EE_{i,j}, \quad \sigma_j = \sqrt{\frac{1}{r} \sum_{i=1}^r (EE_{i,j} - \mu_j)^2}, \quad \mu_j^* = \frac{1}{r} \sum_{i=1}^r |EE_{i,j}|. \quad (8)$$

Where  $\mu_j$  measures the average, overall influence of the input  $j$  on the output;  $\sigma_j$  measures the aggregate degree of higher-order interactions between the  $i$ th factor and all other  $i \neq j$  input factors, known as the

standard deviation of the EE. Finally,  $\mu_i^*$  is an adjusted version of  $\mu_j$  to handle cases when positive and negative effects may cancel one another in  $\mu$  by using the absolute values of EEs [17].

Importance of a variable can be found by comparing  $\mu$  and  $\mu^*$  [84]. Variables with a high value of  $\mu$  suggest a high level of importance and that the effect is monotonic while high values of  $\mu^*$  with low  $\mu$  values indicate non-monotonic and/or non-linear behavior. Variables with an equivalent value of 0 for both  $\mu$  and  $\mu^*$  have no effect on the output and can be discarded. A further comparison of  $\mu^*$  with  $\sigma$  provides information on non-linear and/or interaction effects. High proportions of  $\sigma$  to  $\mu^*$  indicates that the variable interacts with other variables and/or the objective function is non-linear with respect to this variable. Low proportions indicates no interactions and linearity.

Figure 2(a) plots the values of calculated statistics for each of our 5 unknown variables. All five variables have a positive value of  $\mu^*$  and, thus, all five variables have a significant effect on the output. Variables GAMMA\_SERVICE and THETAR\_WORK have the highest importance and influence on the objective function. The value of  $\mu$  and  $\mu^*$  are similar for THETAR\_WORK, suggesting positive monotonic behavior; HBO\_ASC\_TAXI suggests a negative monotonic behavior but the right graph implies an influential non-linear component as well.

Figure 2(b) shows most of the variables have high values of  $\sigma$ , indicating strong interaction effects and/or non-linear behavior. While HBO\_ASC\_TAXI is comparatively lower, its ratio to  $\mu^*$  remains high at 86% of  $\mu^*$ . This indicates a significant interaction or non-linear effect on the other variables but with a lower direct influence on the overall output.

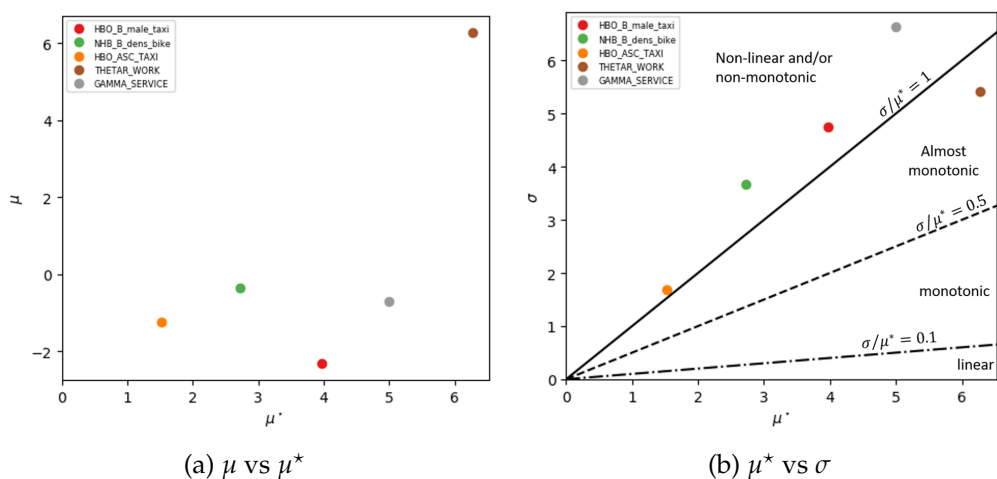


Figure 2: (a) A comparison of  $\mu$  and  $\mu^*$  [84] for importance ranking. Since no variable has a  $\mu^* = 0$ , all variables are significant. (b) A comparison of  $\mu^*$  and  $\sigma$ . High values of  $\mu^*$  with low  $\mu$  values indicate non-monotonic and/or non-linear behavior while high values of  $\sigma$  indicate interactions.

In conclusion, all variables prove important, and the presence of interactions prevent us from using variable screening or shrinkage as a dimensionality reduction technique. Further, the non-linear and non-monotonic nature of the input-output relations advises against using traditional projection-based dimensionality reduction methods, which assume the opposite.

### 3.2 Bayesian Optimization

The Bayesian optimization procedure starts with an initial sample set  $\mathcal{D} = \{\theta^{(i)}, \mathcal{L}(\theta^{(i)})\}_{i=1}^N$ . Two common sample-generating procedures used in computer simulations are the simple random and Latin Hypercube (LHS) sampling techniques [47]. Simple random sampling draws a uniformly-distributed random value from each individual variable's domain to construct a sample set; but, though easier to implement, the procedure cannot guarantee that every portion of the subspace is sampled [47]. LHS first subsections each variable range into equal intervals and selects a random value within each slice before randomly pairing

each variable’s new subset to construct a sample [65]. Our Bayesian optimization procedure uses a LHS configuration to generate our initial sample set.

A surrogate model  $F$  is then estimated using a univariate Gaussian Process to quantify the uncertainty at other unsampled points in the domain; a GP is fully characterized by its mean function  $m$  and its covariance function, or kernel,  $k$  [44].

$$\mathcal{L}(\theta) \sim \mathcal{GP}(m(\theta), k(\theta, \theta')) \quad (9)$$

where

$$\begin{aligned} m(\theta) &= \mathbb{E}[\mathcal{D}|\theta] \\ k(\theta, \theta') &= \mathbb{E}[(\theta - m(\theta))(\theta' - m(\theta'))] \end{aligned} \quad (10)$$

The mean function  $m(\theta)$  is unrestricted but, in practice, routinely assumed to be zero. The correlation equation  $k(\theta, \theta')$  must result in a positive semi-definite matrix; common choices include the Squared Exponential, which is both stationary and isotropic, and the Matérn covariance function, which provides less smoothness through the reduction of the covariance differentiability. General references can be found in [1] and [33]. In this paper, we use the Matérn covariance function:

$$k_{\text{Matern}}(\theta, \theta', \Omega) = \frac{2^{1-v}}{\Gamma(v)} \left[ \frac{\sqrt{2v}|\theta - \theta'|}{\lambda} \right]^v K_v \left[ \frac{\sqrt{2v}|\theta - \theta'|}{\lambda} \right]$$

where  $\Omega = (v, \lambda)$  with lengthscale  $v$  and smoothness  $\lambda$  as non-negative hyperparameters;  $\Gamma$  is the gamma function; and  $K_v$  is a modified Bessel function.

Additionally, we incorporate the inadequacy errors of  $\epsilon(\theta)$  in Equation 1 via a specialized Linear “nugget”  $r(\theta) = \mathcal{N}(0, I\sigma_\epsilon^2)$  [43]:

$$\mathcal{L}(\theta) \sim \mathcal{GP}(m(\theta), K(\theta) = k(\theta, \theta') + r(\theta)I) \quad (11)$$

where  $I$  represents the identity matrix.

Once conditioned on the observed data  $\mathcal{D}$ , the final density known as the posterior distribution, is Normal:

$$[y(\theta) | \mathcal{D}, \theta, \Omega] \sim \mathcal{N}(\mu, \Sigma), \quad (12)$$

where  $\Omega$  are the parameters of the kernel function, and with the following summary statistics:

$$\begin{aligned} \mu &= m(\theta) + k(\theta)(K_{\mathcal{D}})^{-1}(y - m_{\mathcal{D}}) \\ \Sigma &= k(\theta, \theta) + r(\theta) - k(\theta)(K_{\mathcal{D}})^{-1}k(\theta)^T \end{aligned} \quad (13)$$

where  $k(\theta) = (k(\theta, \theta^{(1)}), \dots, k(\theta, \theta^{(N)}))^T$ .

The next step of the BO procedure is the sequential sampling of the input configurations and updating of the parameters of the GP surrogate. Under limited sampling budgets, choosing the next configuration for evaluation  $\theta^{N+1}$  is accomplished using the *optimal experimental design*. The goal is to identify regions of the constrained state space  $\mathcal{A}$  to draw from regions where the loss function  $\mathcal{L}$  is known to have small values (exploitation) or from regions where high uncertainty about the  $\mathcal{L}$  values exist (exploration). The next configuration is chosen using a utility function  $\mathcal{U}$  which captures the exploration-exploitation trade-off required for the given problem. The expectation over the utility function, known as an acquisition function  $a(\theta)$ , is taken over the posterior distribution of the GP surrogate function and minimized to obtain the optimal design choice  $\theta^{N+1}$  [81]:

$$\theta^{N+1} = \arg \max_{\theta \in \theta_\star} a(\theta) = \mathbb{E}[\mathcal{U}(\theta, \Omega)] \quad (14)$$

where  $\theta^{N+1}$  is the optimal input configuration from a pool of potential candidates  $\theta_\star$  in the search space  $\mathcal{A}$ ;  $\mathcal{U}$  is the chosen utility function, and  $\Omega$  represents the hyperparameters of the GP surrogate that approximates the loss function  $\mathcal{L}$ .

Several Bayesian utility functions and their non-Bayesian Design of Experiments (DOE) equivalents are discussed extensively in [19]. For our calibration problem, we use the Expected Improvement (EI) utility function [69], which weighs the value of a proposed sample by the size of its potential improvement to avoid getting stuck in local optima and under-exploration.

$$\mathcal{U}_{EI}(\theta) = \max[0, \mathcal{L}(\theta^*) - \mathcal{L}(\theta)] \quad (15)$$

The final acquisition function is

$$a_{EI}(\theta) = \Sigma[u\Phi(u) + \phi(u)] \quad (16)$$

where  $u = \Sigma^{-1}(\mathcal{L}(\theta^*) - \mu)$ , and  $\Phi$  is the normal cumulative distribution;  $\phi$  is the normal density function, and  $\mathcal{N}(\mathcal{L}; \mu, \Sigma)$  is the predictive posterior distribution.

### 3.3 Dimension Reduction

Although GP surrogates approximate non-linear relations between inputs and outputs well, they are known to fail in higher dimensions. Each increase in dimensionality influences the state-space volume exponentially and, in order for Bayesian Optimisation (BO) to maintain reasonable uncertainty in its predictions, this ‘‘curse of dimensionality’’ would mandate an exponential growth in sample sizes. Parallelization techniques can expand a limited sampling budget, but only by a multiplicative factor; furthermore, when sample sizes grow significantly, the additional computational complexity within the algorithm itself becomes a hindrance. For this reason, BO is typically ineffective beyond a moderate level of high-dimensional complexity [82] when resources are limited. However, if the dimensionality issue can be addressed, BO would become viable again.

Because the relationship between inputs and outputs varies primarily along a small set of curves in many engineering applications, dimensional reduction is a common approach to solve the issue of high-dimensional statespaces. Projection-based techniques find a condensed representation of the dataset in a lower-dimensional subspace and have traditionally been implemented due to their computational and interpretable ease. For linear instances, common techniques include Principal Component Analysis (PCA), Partial Least Squares (PLS), or various single-index models. Of particular popularity in engineering disciplines, the method known as Active Subspaces (AS) projects the data along influential directions known as Principal Components (PCs). Utilizing derivatives, the algorithm identifies the necessary linear combinations to produce a lower-dimensional subspace. For further details of Active Subspaces, see Appendix A.

As we demonstrated in Section 3.1, our ABM exhibits non-linear and significant interactions which would be lost by using these popular linear dimensionality reduction techniques. We propose a non-linear extension of the projection-based methods. Our dimensionality reduction procedures find a map  $\phi(\theta) \rightarrow \psi$  that transforms the input vector  $\theta$  into a lower-dimensional vector of latent variables  $\psi$ . We propose using a Deep Learning (DL) architecture to construct the nonlinear mapping  $\phi$ . Our paper will use Active Subspaces as a benchmark for demonstration.

Deep learners are a class of non-linear functions which construct a predictive mapping using hierarchical layers of latent variables. The output can be a continuous, discrete, or mixed value set. Each layer  $\ell$  applies element-wise a univariate activation function  $\tau$  to an affine transformation:

$$\begin{aligned} Z^{(1)} &= \tau^{(1)} \left( W^{(0)}\Theta + b^{(0)} \right), \\ &\dots \\ Z^{(\ell)} &= \tau^{(\ell)} \left( W^{(\ell-1)}Z^{(\ell-1)} + b^{(\ell-1)} \right), \\ \hat{Y} &= W^\ell Z^\ell + b^{(\ell)}, \end{aligned} \quad (17)$$

where  $W$  represents the weights placed on the layer’s input set  $Z$ , and  $b$  represents the offset value critical to recovering shifted multivariate functions. Given the number of layers  $\ell$ , a predictor is a result of the composite map

$$\hat{\mathcal{L}} := \left( \tau_1^{W_1, b_1} \circ \dots \circ \tau_\ell^{W_\ell, b_\ell} \right) (\theta). \quad (18)$$

The general approximation capabilities of deep learning networks is rooted in the universal basis theorem proved by Kolmogorov [55]. As data progresses down the network, each layer applies a folding operator to predecessor’s divided space according to the chosen activation function  $\tau$ . Cybenko[27] proved that a fully-connected network with a single hidden layer and sigmoid activation function can uniformly approximate any continuous multivariate function on a bounded domain within an error margin; further work documented similar results for additional classes of activation functions [9, 50, 39] and eventually led to deep learning networks being deemed universal approximators: a single-layered deep learning network with a suitable activation function for continuous functions; a two-layered version for discontinuous and Boolean functions.

Deep learning multi-layered networks designed for dimensionality reduction learning must contain at least one layer  $Z^{(i)} \in \mathbb{R}^q$  with fewer nodes than the input  $q \ll d$  layer. This bottleneck layer forces the network to learn a compressed, or lower dimensional, set of latent features describing the input-output relationship. We use this representational form to extract a vector representation  $\psi$  within one of the deep learner’s hidden layers.

However, to be applicable to our BO framework, our dimensionality reduction technique must be capable of reconstructing a point in the original input space from any point in the latent space. This inversion of the projection map is a non-trivial task for non-linear mappings and is why linear approximation techniques have dominate the field of dimensionality reduction, despite commonly mapping non-linear relationships [56]. We overcome this translation obstacle by incorporating an additional deep learning multi-layered network mapping  $s(\psi) \rightarrow \hat{\theta}$  to reconstruct the input vector  $\theta$  from the latent variable set  $\psi, q \ll d$ .

The two networks share the same initial layers up to the reduced dimensional layer, as shown in Figure 3, in order to enforce they both use the same encoding substructure.

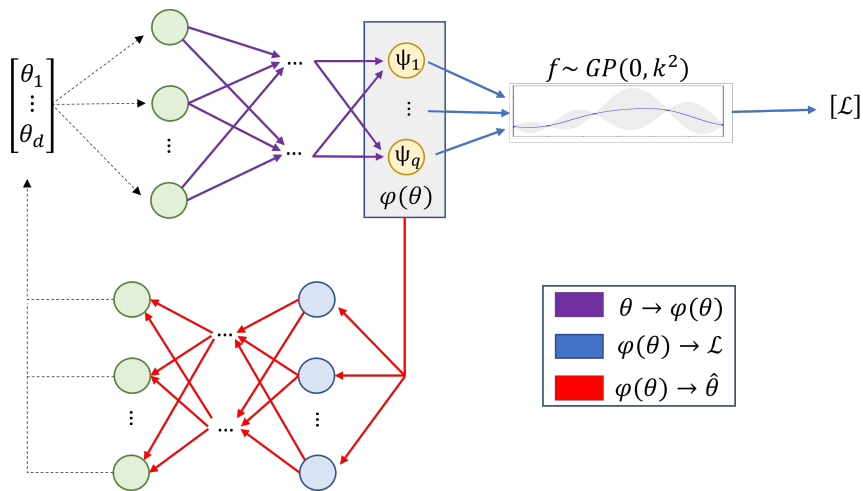


Figure 3: Graphical Representation of the Combinatorial Deep Learning Multi-Layer Network for Calibration

### 3.4 Combined Model

The final architecture is then combines dimensionality reduction and GP to approximate the loss function  $\mathcal{L}$  and is given by the following equations

$$\psi = \phi_{W_A}(\theta) \quad (19)$$

$$\hat{\theta} = s_{W_B}(\psi) \quad (20)$$

$$\mathcal{L} \sim \mathcal{GP}(m(\psi), K(\psi, \psi')). \quad (21)$$

We define an estimation procedure that jointly estimates the parameters of the deep learning transformation, the basis vectors and hyperparameters of the univariate GPs. Training is accomplished by minimizing

a combined training function  $\zeta(\theta)$  which takes into account both the errors in the predicted output's loss values  $\hat{\mathcal{L}}$  and the reconstructed input values  $\hat{\theta}$ . This joint training of the encoder and decoder allows us to efficiently perform cross validation on the dimensionality of the latent space.

Though any function which captures these errors can be used, this paper's training function minimizes the Mean Squared Error (MSE) between  $\hat{\mathcal{L}}$  and  $\mathcal{L}$  multiplied by a scaler  $\lambda$  and a Mean Squared Error (MSE) function along with a summed quadratic penalty cost  $P$  for producing reconstructed values  $\hat{\theta}$  outside of the original subspace bounds:

$$\zeta(\theta) = -\lambda \sum_{i=1}^N (\mathcal{L}_i - \hat{\mathcal{L}}_i)^2 + \sum_{i=1}^N \left[ (\theta^{(i)} - \hat{\theta}^{(i)})^2 + P \left( \max[0, \theta^{(i)} - \theta_{ub}]^2 + \max[0, \theta_{lb} - \theta^{(i)}]^2 \right) \right], \quad (22)$$

where  $\lambda$  represents the importance weight of the encoder verses the decoder portion;  $P$  is the penalty cost for producing predicted values outside of the original subspace bounds;  $\theta_{ub}$  represents the input set's upper bound; and  $\theta_{lb}$  represents the input set's lower bound.

Note, due to the bounded requirement of BO, some activation functions will require adjustments for at least the dimension-reducing bottleneck layer. For example, the ReLU function can be bounded by adjusting the deep learner to add two new parameters defining the state space bounds  $DR_{ub}, DR_{lb}$ :

$$U(\theta^{N+1}) = \begin{cases} DR_{lb}, & \theta < DR_{lb} \\ \theta, & DR_{lb} \leq \theta \leq DR_{lb} \\ DR_{ub}, & \theta > DR_{ub} \end{cases} \quad (23)$$

When constructing the deep learning architecture, the user should consider that any artificial bounding can result in the need for additional nodes and/or layers when compared with an unbounded version.

### 3.5 Parallelization

Traditional Bayesian optimization algorithms are sequential in nature [51]; however, when high-dimensional simulation runs take hours or days, maximizing the number of samples become critical to optimization efforts. Several recent approaches address the problem of limited calibration times through parallel evaluations [102, 25, 29, 89, 100] using High Performance Computing (HPC).

We incorporate this parallel approach into our computational framework by adding a HPC master controller program to coordinate worker units which run codes across multiple processors concurrently; the result being a larger set of recommended samples within the same limited time frame. Note that, for this optimization framework, the controller must also interact with a model exploration program for its queue of untested input sets, as shown in Figure 4.

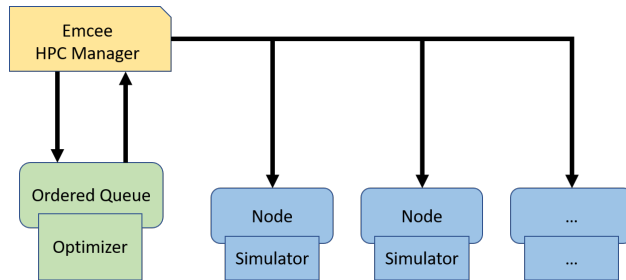


Figure 4: Computation Framework for HPC

In direct consequence of parallelism, BO must also be adjusted to recommend multiple samples. A natural approach may seem to be simply choosing the top  $c$  candidates of the acquisition function  $a(\theta)$ . However, the problem of that approach lies in the assumption that the top set of points depict unique sections of the search space and are not clustered together. This assumption is false. It is not uncommon that, when a new portion of the search space is deemed worth exploring, many of the candidates in that

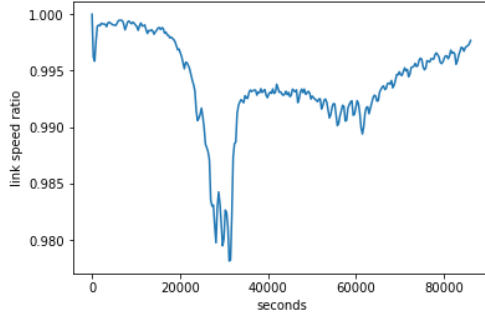


Figure 5: Traffic Congestion Dependence upon Time

region will contain a large acquisition value, as they all are deemed equally valuable for learning the area’s structure.

Instead, the expected information gained from evaluating a selected candidate within a batch of size  $n_b$  can be leveraged when deciding the next option. In this approach, the posterior distribution is updated with a pseudo-sample  $\hat{\mathcal{L}}$  created from the predicted mean  $\mu$  for the chosen candidate  $\theta^{(N+1)}_{i, i=1, \dots, n_b}$ . This expected “information gain” now prevents additional candidates from clustering; the posterior distribution is updated before for all subsequent candidates in the batch are chosen.

While proven successful enough to be the most common method implemented[102], this expectation method is not the only possible recourse. Recently, more complex methods have begun to be explored that may prove, in some optimization scenarios where batch sizes are expected to be very large, to be more useful:

- Gradient applications which choose the next sample by maximizing the expected incremental value [102], value of information [103], or other methods of diversity measurements [5]
- Utilizing the lower bound for the previously-chosen but yet-to-evaluate samples [103]
- Partitioning the search space via some design such as treed maximum entropy and selecting candidates from each region proportional to the volume in the region [42]
- Performing Monte-Carlo simulation to estimate the posterior distribution over examples selected by the sequential method and then select a batch of  $c$  examples that “best matches” this distribution; however, no theoretical results prove convergence [5]

### 3.6 Adjusted Mean Function

Thus far, the influential relationship between traffic congestion and time, depicted in Figure 5, has not been explicitly addressed.

The univariate objective function  $\mathcal{L}$  has averaged out the variance across the time dimension and, while the deep learning dimension reduction technique is trained without doing so, the Active Subspace Dimensionality Reduction is not.

We propose leveraging the multivariate capability of deep learning network outputs with the structural influence of a non-zero mean function  $m$ , not typically used in typical GP applications. Recall in Equation 12, a non-zero mean  $m(\theta)$  will not only influence the predictive posterior’s mean  $\mu$ , but also the predictive posterior’s covariance  $\Sigma$  structure. In addition, because the EI acquisition function  $a$  also relies heavily on the predicted mean of a potential candidate, discarding the typical zero-mean assumption will have a critical impact on a candidate’s recommendation. Indeed, an educated mean function  $\mu_{DL}$  which can provide additional relational information to the distinct application of interest allows for a broadly useful and influential enhancement.

In this paper, we propose using a simple deep learning multi-layered network structure to explicitly capture a deterministic [76] mean approximation of the surrogate function in relation to time:

$$\mathcal{L}(\theta) \sim \mathcal{GP}(m_{DL}(\theta), K(\theta, \theta')) \quad (24)$$

## 4 Empirical Results

We demonstrate our methodology on a series of simulated examples and then apply it to minimize the ABM calibration objective loss function  $\mathcal{L}$ , which is the mean squared difference between the observed and simulated turn travel times for every 5-minute interval across a 24-hour period.

### 4.1 Dimensionality Reduction of Simulated Data

We begin by demonstrating the quality of our dimensionality reduction approach on two simulated examples (linear and non-linear). Quality of reconstruction from the reduced space is essential for our calibration algorithm. If unsuccessful, the associated reduction method will likely hinder the optimization algorithm. Therefore, we demonstrate the bi-directional translation of our pre-processing dimension reduction structure on a simple linear and non-linear simulation set with known lower-dimensional structures. Both examples draw on problems from [37]. In this Section, we compare our dimensionality reduction approach with a state-of-the-art technique, called Active Subspace, which is described in an Appendix.

For both examples, we use a set of  $n_{train} = 80$  training samples for learning the encoders and decoders and  $n_{test} = 200$  testing samples to assess quality of reconstruction. Both training and testing samples are generated using Latin Hypercube sampling. For the Active Subspace technique, we use the author’s recommended local linear approximation documented in [24], which uses least-squares to fit the coefficients  $\hat{\beta}_0$  and  $\hat{\beta}$  of the model:

$$\mathcal{L}(\theta) \approx \hat{\beta}_0 + \hat{\beta}^T \theta.$$

Then, the gradient required for Active Subspace is approximated as  $\nabla_{\theta} \mathcal{L}(\theta) = \hat{\beta}$ . In addition, 500 bootstraps are used for each example and we execute the radial basis response surface code from the Active Subspaces Python package produced by the method authors to map the relationship between reduced input vector  $\psi_{AS}$  and the true function output  $y$ . Lastly, to provide benchmark comparisons, and because Active Subspaces is the only method which requires self-determination of the dimensional size of its reduced subspace, this paper uses the final Active Subspace dimension as the limit  $k_{max}$  which the deep learning model can project up to. Each example will note the dimensions.

#### 4.1.1 Linear Function

The first example has linear simulated response  $y$ , a 1-dimensional output, given a 10-dimensional input set  $\theta = [\theta_1, \dots, \theta_{10}]$  between  $[0, 1]$ :

$$\begin{aligned} \mathcal{L}(\theta) &= \sum_{i=1}^4 0.2\theta_i + 0\theta_5 + 0\theta_6 + 0\theta_7 + 0\theta_8 + 0\theta_9 + 0\theta_{10} + e \\ e &\sim \mathcal{N}(0, 0.05^2) \end{aligned} \quad (25)$$

In this manner, a lower-dimensional representation of the input data is guaranteed to be producible. The Active Subspace method *AS* found a significant ‘gap’ between the first and second subspace dimensions, as shown in Figure 6(a), and, therefore, determined its dimension set to be  $k = 1$ ; the linear trend in Figure 6(b) and the second dimension’s lack of influence over the first, displayed in Figure 6(c), corroborates this conclusion. As a result, our proposed deep learning model must also use  $k = 1$  dimensions for this problem.

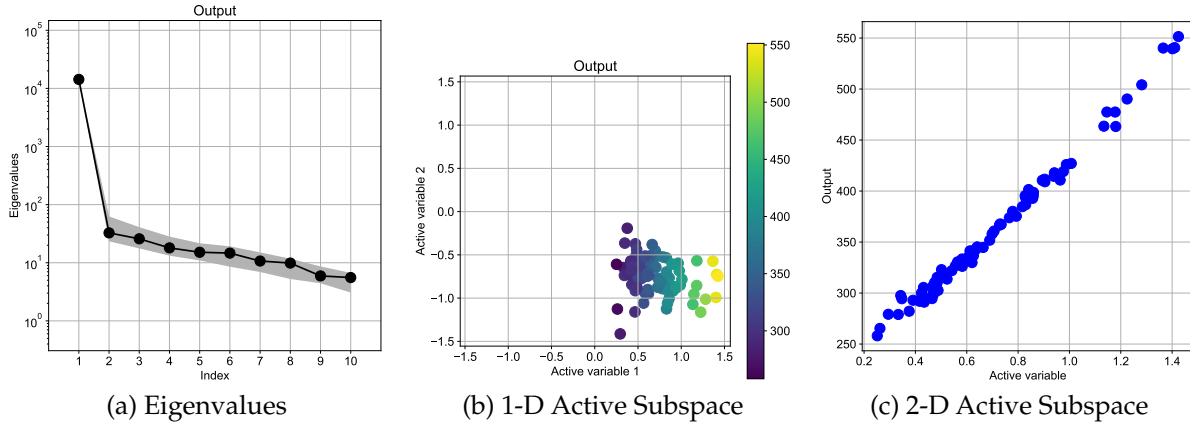
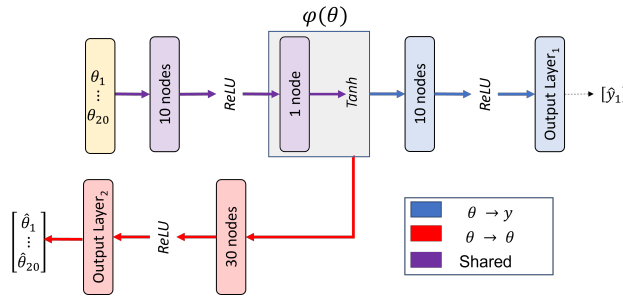


Figure 6: (a) visualizes the eigenvalues of each eigenvector; the significant separation between the first and second index indicates a single dimensional active subspace (b) illustrates the output trend over a varying 1-D active subspace; the linear trend signifies a 1-D subspace is successful (c) illustrates the output trend over a varying 2-D active subspace; the output shows to only be influenced by the first active subspace regardless of the second's change in values.

For the deep learning technique  $DL$ , a simple multi-layered network trained on 1000 epochs with learning rate  $\alpha = 0.01$  and seed=13 is used with the following structure:



We set  $\lambda = 100$ ,  $P = 100$  to make decoding and encoding equally important.

The authors would like to note that the same results can be found using a purely linear deep learner with a learning rate of  $\alpha = 0.001$ :

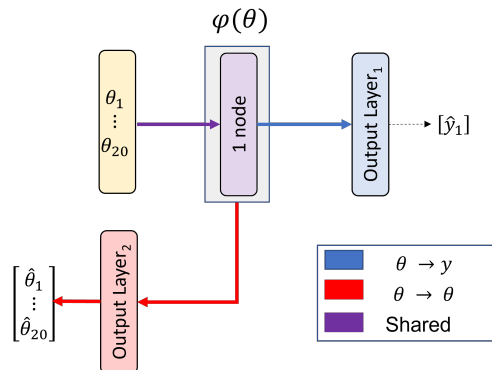


Figure 8: Alternative Example 1 Deep Learner Multi-layered Network Structure

The non-linear version is used, however, to demonstrate and emphasize that a nonlinear neural network is still capable of capturing a linear relationship.

To begin, we look at how well the predicted outputs  $\hat{y}$  align with the true outputs  $y$  for each method. Shown in Figure 9, the two methods provide similar results with a MSE of 0.0033 for the *AS* method and 0.0034 for the *DL* method. However, the *DL* method produces stronger predictions about the center of the statespace, where most of the samples concentrate, while *AS* produces more accurate predictions at either end. This behavior is likely reflective of how the two subspaces are found: *AS* seeks the directions of average variability across the entire statespace; *DL* wants to minimize its error among the bulk of samples.

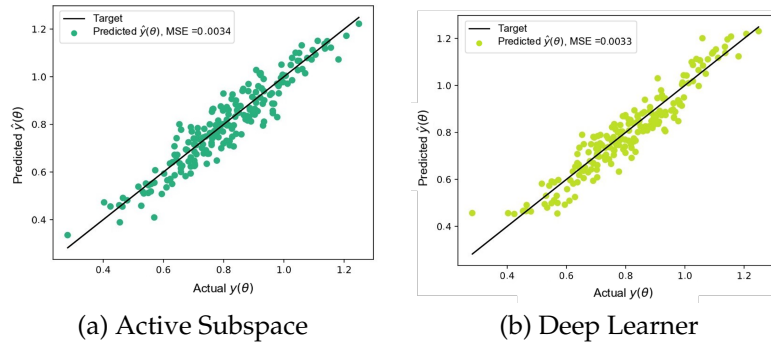


Figure 9: Comparing the accuracy of the (a) *AS* dimension reduction architecture and (b) *DL* dimension reduction architecture's predictions for  $y$ . The Mean Squared Error (MSE) provides benchmark comparisons while the black line indicates the correct position if  $\hat{y}(\theta) = y(\theta)$ .

Having set the importance of learning the encoding equal to decoding while training, we would expect similar success when analyzing the accuracy of the methods' decoder. To check, we first decode the encoded lower-dimensional representations  $\psi$  into estimated reconstructions  $\hat{\theta}$  and then evaluate them through the true function,  $Y(\hat{\theta})$ . We take this approach because multiple samples can produce the same output, making their lower representation indistinguishable. For this reason, the decoded input is unlikely to match the original inputs exactly, but should be expected to produce the same outcomes when run through the true function.

Note, the true  $\theta$  values are simultaneously re-evaluated in the simulator with the reconstructed  $\hat{\theta}$  to ensure they share the exact random error; this way, a perfect match would be reflected at  $Y\hat{\theta} = Y\theta$ . The results are shown in Figure 10 and, as expected, similar success is found with an MSE of 0.0009 for the *AS* method and 0.001 for the *DL* method.

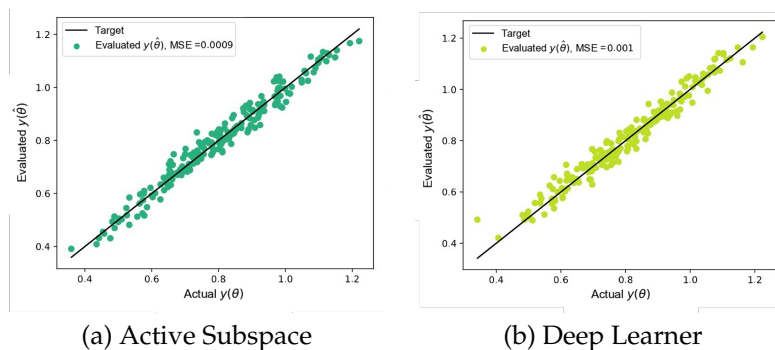


Figure 10: Comparing the success of the (a) *AS* dimension reduction decoder and (b) *DL* dimension reduction decoder in capturing non-linearity by comparing the simulated outputs given the decoded inputs  $y(\hat{\theta})$  and the simulated output given the original inputs  $y(\theta)$ . The Mean Squared Error (MSE) provides benchmark comparisons while the black line indicates the correct position if  $y(\hat{\theta}) = y(\theta)$  and capturing non-linearity was successful.

Finally, Figure 11 shows what a zero-mean GP built over the two reduced subspaces, referred as  $AS + \mathcal{GP}_0$  and  $DL + \mathcal{GP}_0$ , would predict for our 200 test data points and further compare them with a zero-mean GP built over the original subspace  $Original + \mathcal{GP}_0$ , i.e. without any dimension reduction pre-processing. To provide quantified context across the three GPs instances, the authors offer both the number of points which lie outside of the predicted 95% Confidence Intervals graphed in red, and a 'distance' value describing the magnitude difference of the various predictive Confidence Intervals against the true one.

$$\text{BoundaryDistance}_{DR} = \sum_{i=0}^{200} \frac{\sqrt{(\hat{LB}_{DR}(\theta^{(i)}) - y^{(i)})^2} + \sqrt{(\hat{UB}_{DR}(\theta^{(i)}) - y^{(i)})^2}}{\sqrt{(LB(\theta^{(i)}) - y^{(i)})^2} + \sqrt{(UB(\theta^{(i)}) - y^{(i)})^2}} \quad (26)$$

where  $\hat{LB}, \hat{UB}$  are the estimated bounds of the predicted confidence interval produced by the GP built on dimension reduction technique  $DR$ ;  $LB, UB$  are the true bounds based on the problem, and  $\theta^{(i)}, y^{(i)}$  are the test data sets.

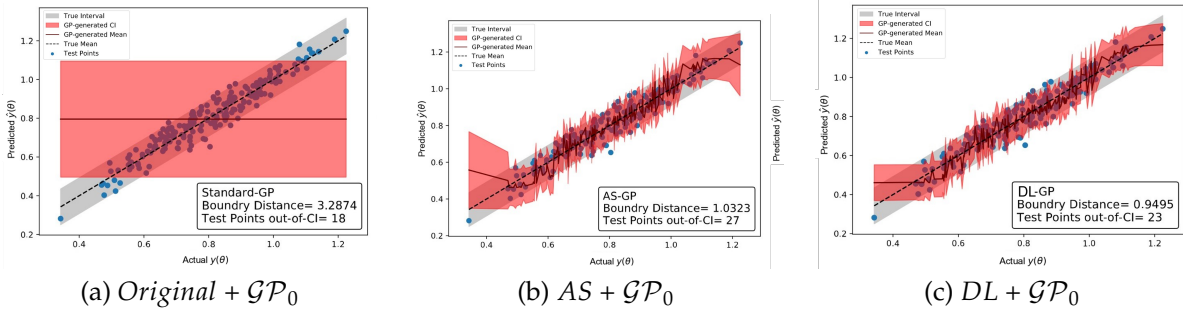


Figure 11: Comparison of  $n_{test} = 200$  test predictions by a constructed GP based on each reduction method with the true values. Since the true function is stochastic, the true values are captured as follows: the black line indicates the correct position if the predicted value mean matches the true mean; the gray shaded region indicates the true function's 95% Confidence Interval; and the blue points are the evaluations provided as test data. The red line represents the mean predicted value of the GP; the red shaded region indicates the GP's 95% Confidence Interval. The GP is built based on only the training set  $n_{train} = 80$ .

Most notably, both pre-processing methods achieve dramatic improvements to the GP built using the original 10-dimensional state-space  $Original + \mathcal{GP}_0$ , highlighting the advantage of our projection-based approach. Despite its more accurate predictions  $\hat{y}$  at the tail ends of the statespace, the  $AS + \mathcal{GP}_0$  build is unexpectedly less confident; and, its predicted mean veers more significantly from true average than the  $DL + \mathcal{GP}_0$ . Due to the volume of samples clustered in the middle, this divergence is only hinted at by the slight difference in the distance calculation of 1.0323 for  $AS + \mathcal{GP}_0$  and 0.9495 for  $DL + \mathcal{GP}_0$ .

#### 4.1.2 Non-linear Prediction

The second example produces a non-linear simulated response  $y$ , a 1-dimensional output, from a 10-dimensional input set  $\theta = [\theta_1, \dots, \theta_{10}]$ :

$$\begin{aligned} \mathcal{L}(\theta) &= \sin(\theta_1) + \sin(5\theta_2) + 0\theta_3 + 0\theta_4 + 0\theta_5 + 0\theta_6 + 0\theta_7 + 0\theta_8 + 0\theta_9 + 0\theta_{10} + e \\ e &\sim \mathcal{N}(0, 0.05^2) \end{aligned} \quad (27)$$

The Active Subspace method determined a dimension set of  $k = 2$ , as shown in Figure 12.

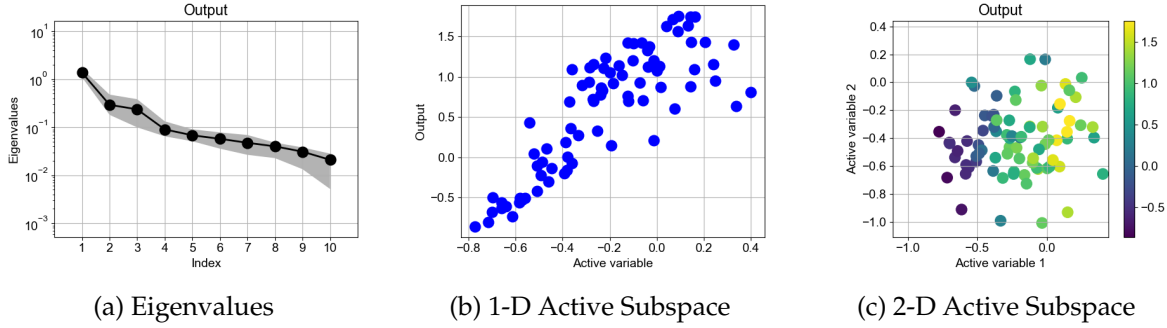


Figure 12: (a) visualizes the eigenvalues of each eigenvector; the significant separation between the first and second index indicates a single dimensional active subspace. However, the (b) 1-D active subspace illustrates the output trend is not linear and that the second index may be necessary. (c) illustrates the output trend over a varying 2-D active subspace; the output supports the use of two active subspaces.

Our deep learner uses a learning rate  $\alpha = 0.01$  and  $seed = 88$  under the following structure:

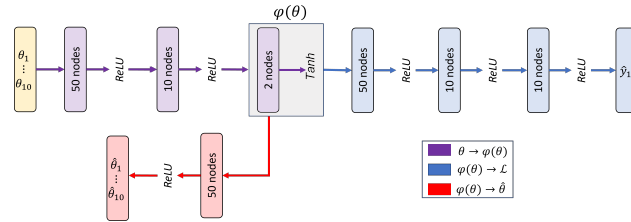


Figure 13: Example 2 Neural Network Structure

By setting  $\lambda = 10$ , we again make decoding and encoding equally important.

Figure 14 displays the results of predicting the output  $\hat{y}$  from each method's lower-dimensional transformation  $psi$ .

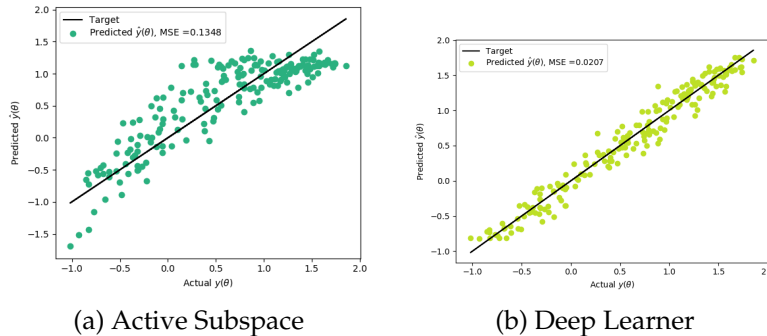


Figure 14: Comparing the accuracy of the (a) AS dimension reduction architecture and (b) DL dimension reduction architecture's predictions for  $y$ . The Mean Squared Error (MSE) provides benchmark comparisons while the black line indicates the correct position if  $\hat{y}(\theta) = y(\theta)$ .

The curved effect seen in the Figure 14(a) is the consequence of the AS technique's difficulty with capturing the non-linear behavior of the problem; the DL method, on the other hand, performs exceedingly well, producing predictions clustered about the true values for the entire domain.

Figure 15 displays the results of the simulated outcomes using each method's decoded input set  $y(\hat{\theta})$ . The DL method remains strong in its reconstruction capabilities, with a similar MSE of 0.02 while the AS

method continues to have difficulty with the problem, though the more obvious curvature of the predictive outputs is absent.

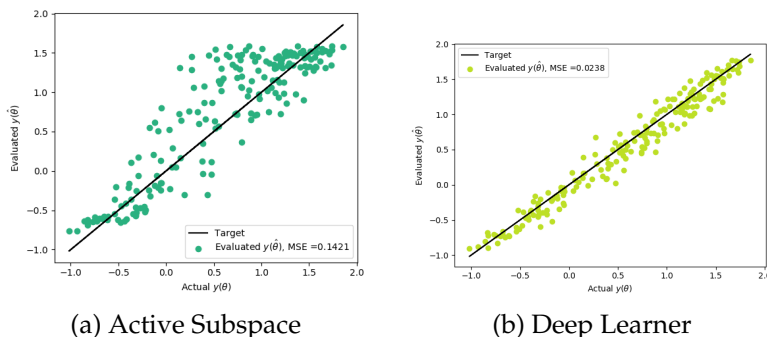


Figure 15: Comparing the success of the (a) *AS* dimension reduction decoder and (b) *DL* dimension reduction decoder in capturing non-linearity by comparing the simulated outputs given the decoded inputs  $y(\hat{\theta})$  and the simulated output given the original inputs  $y(\theta)$ . The Mean Squared Error (MSE) provides benchmark comparisons while the black line indicates the correct position if  $y(\hat{\theta}) = y(\theta)$  and capturing non-linearity was successful.

Lastly, we repeat the previous example’s final analysis via Figure 11 to show what a zero-mean GP built over the two reduced subspaces, referred as  $AS + \mathcal{GP}_0$  and  $DL + \mathcal{GP}_0$ , would predict for our 200 test data points and further compare them with a zero-mean GP built over the original subspace *Original* +  $\mathcal{GP}_0$ , i.e. without any dimension reduction pre-processing.

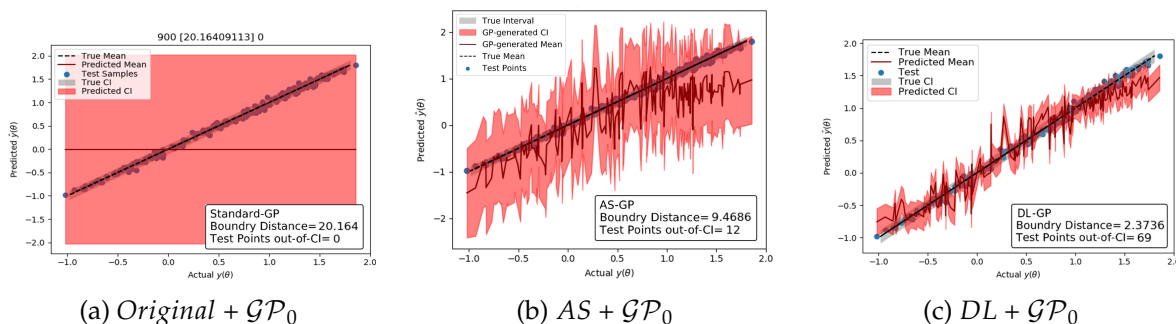


Figure 16: Comparison of  $n_{test} = 200$  test predictions by a constructed GP based on each reduction method with the true values. Since the true function is stochastic, the true values are captured as follows: the black line indicates the correct position if the predicted value mean matches the true mean; the gray shaded region indicates the true function’s 95% Confidence Interval; and the blue points are the evaluations provided as test data. The red line represents the mean predicted value of the GP; the red shaded region indicates the GP’s 95% Confidence Interval. The GP is built based on only the training set  $n_{train} = 80$ .

Again the difference between the reduction methods and the original algorithm are quite obvious, again highlighting the advantage of our projection-based approach. Additionally, the magnitude in difference in the uncertainty of the  $AS + \mathcal{GP}_0$  method, along with the repeated curvature seen in the *AS* method’s original prediction graph (Figure 15), demonstrate the importance for having a non-linear dimension reducer when encountering non-linear problems.

## 4.2 ABM Calibration

We demonstrate our framework using the POLARIS ABM model for ground transportation. We demonstrate the methodology introduced in this paper by calibrating key parameters of the POLARIS ABM model

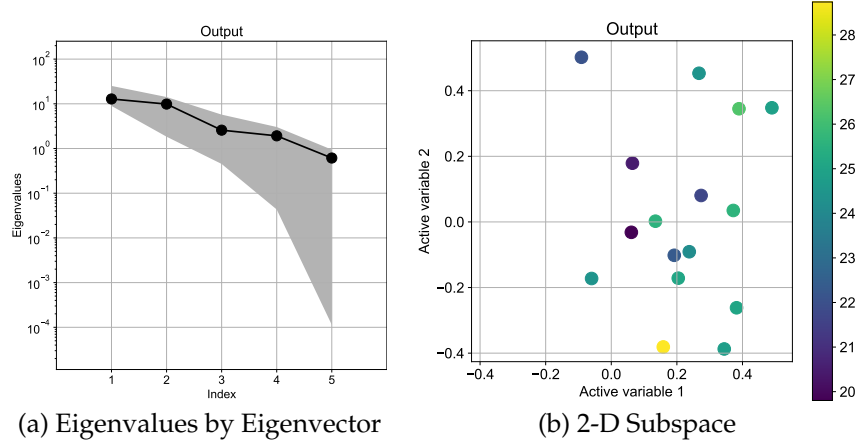


Figure 17: (a) Eigenvalues for each variable Eigenvector (black circles) and accompanying Bootstrap Interval (grey regions) found using 1000 bootstrap replicates. (b) Training samples projected onto the 2-D active subspace.

of ground transportation in Bloomington, Illinois. All variables not being calibrated are assumed to be known. We generate an initial sample of size  $N = 16$ , which is used to estimate the parameters of our dimensionality reduction maps, as well as the parameters of the mean function. The initial sample set was generated via Latin Hypercube. Then we apply BO with and without a dimensionality reduction pre-processing step. Specifically we evaluated the following dimensionality reduction configurations:

- **Original** (*Original*)- no dimensionality reduction
- **Active Subspace** (*AS*) - the 2-dimensional subspace resulting from the Active Subspace dimensionality reduction pre-processing outlined in Appendix A
- **Deep Learning Multi-layer Network** (*DL*) - the 3-dimensional subspace resulting from the deep learning dimensionality reduction pre-processing.

Then we combine each of the dimensionality reduction configuration with one of the two GP profiles: a zero-mean GP  $\mathcal{GP}_0$ , and a deep learning multi-layered network-adjusted mean GP  $\mathcal{GP}_{DL}$ . Both instances use a Matérn covariance function.

The choice of latent space dimensionality for the *AS* algorithm was determined from the elbow plot shown in Figure 17(a), which shows the eigenvalues and the 95% confidence interval calculated from 1000 bootstrap samples.

The gap between the second and third variables indicate the likely presence of a 2-dimensional active subspace, which is supported by Figure 17(b). Notably, the bounds in the bootstrap intervals are quite large; however, given that the bootstrap intervals are most bias at low sample numbers, this outcome is not unexpected.

A 3-dimensional subspace was constructed for the *DL* dimension reduction algorithm using the structure visualized in Figure 18.

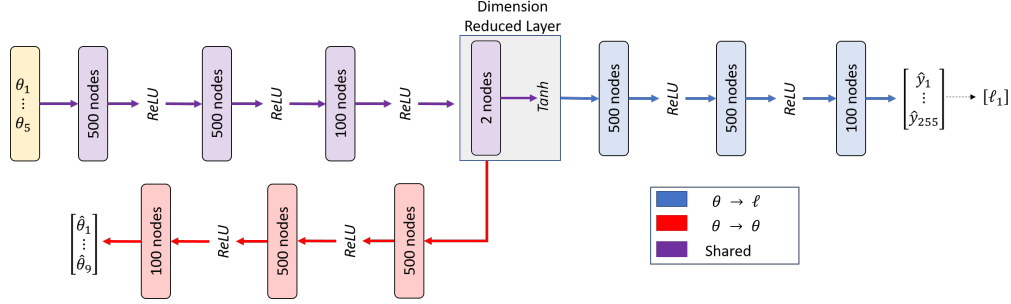


Figure 18: The implemented  $DL$  structure for calibration. Rectangles represent the number of affine transformations applied to their layer inputs.

A  $ReLU$  function was applied universally with the exception of the reduced dimension layer, which utilized a  $\tanh$  transformation to enforce a range boundary. The network was trained on 1000 epochs with a training function  $R(\theta)_{DL}$  using a penalty value of  $P = 200$  for decoding outside the original subspace bounds and a scalar  $\lambda = 0.005$  in order to encourage equal consideration between learning the decoding and encoding structures:

$$R_{DL}(\theta) = 0.005 \|\mathcal{L} - \hat{\mathcal{L}}\|_F + \|\theta - \hat{\theta}\|_F + 200 \sum_{i=1}^N \left[ \max[0, \hat{\theta}_i - \theta_{ui}]^2 + \max[0, \theta_{li} - \hat{\theta}_i]^2 \right] \quad (28)$$

Each subspace method, the same deep learner mean structure was used for the modified BO GP, depicted in 19.

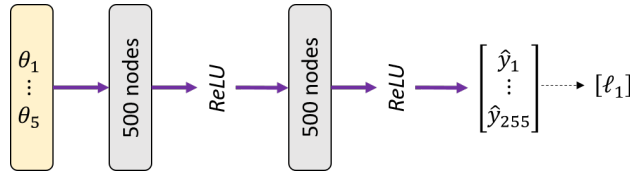


Figure 19: The implemented network structure of the adjusted mean function. The rectangles represent the affine transformations applied to their layer inputs.

A  $ReLU$  function was applied universally and the network was trained on 800 epochs with a learning rate of 0.01; a simple MSE loss function was used along with an Expected Improvement (EI) utility criterion with batch-size of 2.

Now we apply our Bayesian Optimisation algorithm described in Section 3.2 to the problem of calibrating the five parameters given in Table 1. We compare the performance of BO without dimensionality reduction, and with zero mean ( $Original + \mathcal{GP}_0$ ), as well as with the non-linear mean function defined by a deep learning multi-layered network ( $Original + \mathcal{GP}_{DL}$ ). Further, we evaluate the effect of two dimensionality reduction techniques on the convergence of our algorithm.

Figure 20 shows the value of the objective function  $\mathcal{L}$  for six different variations of our optimisation algorithm.

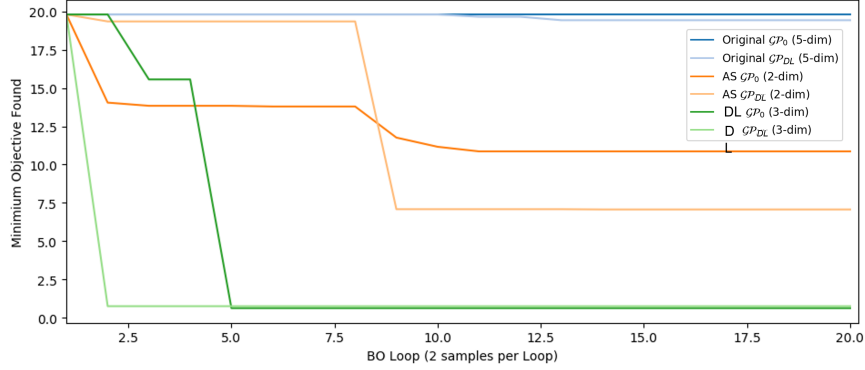


Figure 20: Comparison of the minimum objective value found in 20 BO iterations by each configuration during the calibration of 5 dimensions.

Although vanilla BO is usually applicable to 5-dimensional problems, the highly non-linear and heteroskedastic nature of our problem makes this BO approach impractical. The *Original* +  $\mathcal{GP}_0$  BO yields no improvements after 20 iterations. When the non-zero DL mean was used *Original* +  $\mathcal{GP}_{DL}$ , the BO only manages an 2% improvement after 12 iterations.

The  $AS + \mathcal{GP}_0$  configuration achieves a 30% objective reduction within the first iterations; within 10 iterations, it ultimately settles at an objective value of 10.86 for a total improvement of 45% and then stagnates. Adding a  $\mathcal{GP}_{DL}$  mean improves on the  $AS + \mathcal{GP}_0$  result by 35%, leading to a final objective value of 7.07 and a 65% final improvement on the initial solution. However, it required 6 more iterations for  $AS + \mathcal{GP}_{DL}$  to achieve the improvement.

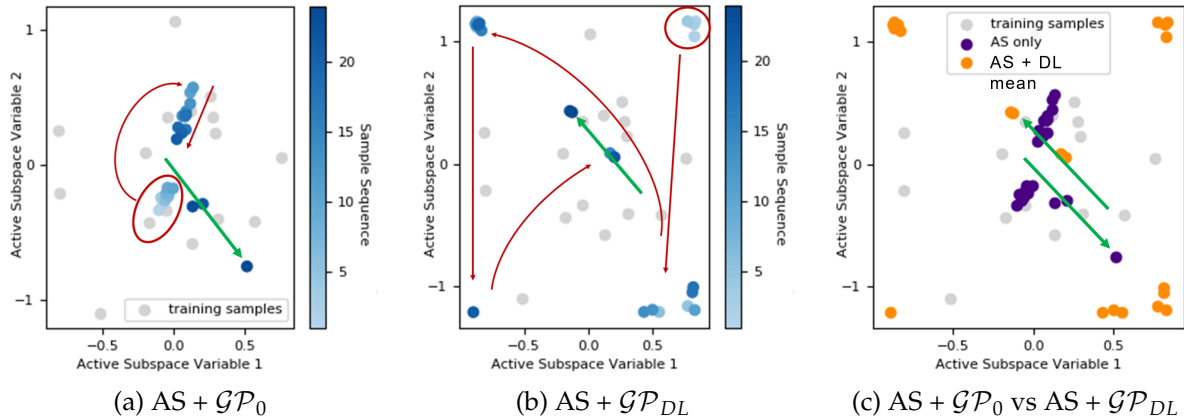


Figure 21: Samples in latent subspace that were used by the search algorithm. The grey dots correspond to the initial 16 samples and the 40 colored dots were sequentially recommended in over the 20 BO iterations. The intensity of the blue color corresponds to the order in which the samples were recommended. The red circles are initial recommendations, the red arrows show the sampling directions, and the green arrow highlights the final trajectory. (a)  $AS + \mathcal{GP}_0$  (b)  $AS + \mathcal{GP}_{DL}$  (c) overlays (a) in purple and (b) in orange to highlight that the final trajectories are parallel but offset.

Figure 21 shows that the use of the  $\mathcal{GP}_{DL}$  leads to more exploration by the search algorithm. While,  $AS + \mathcal{GP}_0$  primarily employed exploitation of the initial training set, recommending samplings within a tight cluster about the majority of the training points in the center of the subspace, the  $AS + \mathcal{GP}_{DL}$  explored the unknown portions of the search space.

Typically, the change in behavior would imply that the Expected Improvement (EI) acquisition function faced higher variance due to the DL mean as, broadly, EI encourages exploitation when a strong reduction

in the mean function is predicted and exploration when the variance is high. However, as shown in Figure 22, this is not the case.

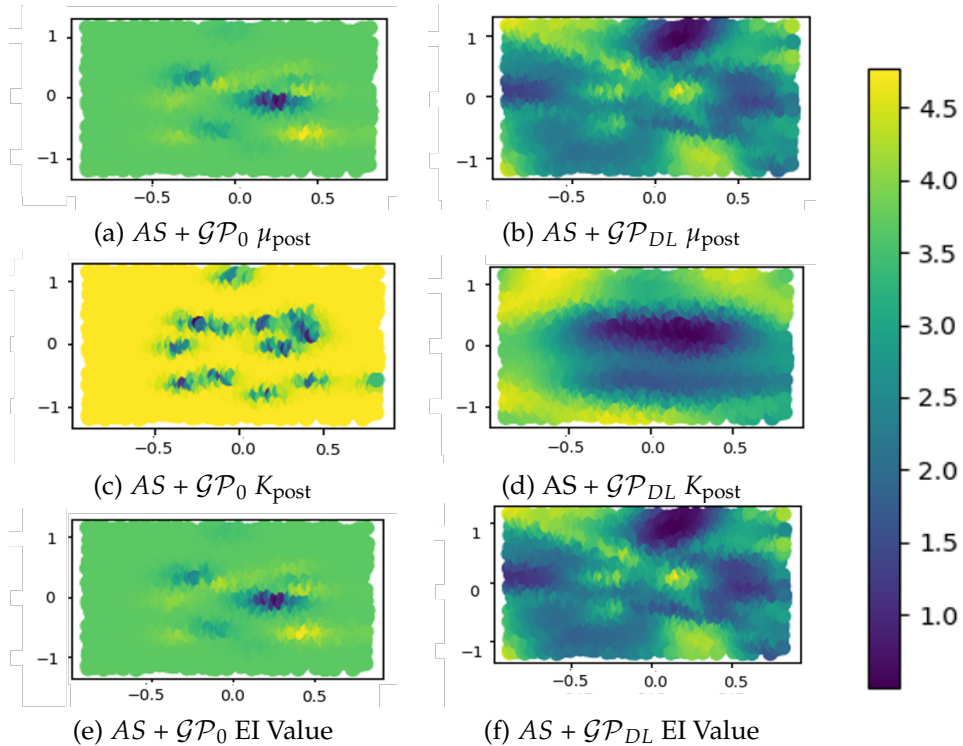


Figure 22: Expected Improvement components and acquisition values for candidate points in the  $AS$  state-space during an interval of the BO calibration for  $AS + \mathcal{GP}_0$  (a)(c)(e) and  $AS + \mathcal{GP}_{DL}$  (b)(d)(f). (a) and (b) show the predicted mean reduction component, (c) and (d) show the predicted standard deviation component, and (e) and (f) show the final acquisition calculation result. The acquisition function in both settings rely heavily on the mean reduction component despite their diverging recommendation patterns.

While both  $\mathcal{GP}_0$  and  $\mathcal{GP}_{DL}$  acquisition values clearly rely heavily on the potential in mean reduction, it is the landscape of the predicted mean and uncertainty which shifts significantly. This outcome is likely due to the newly reflected magnitude of non-linear behaviors previously unaddressed by the  $AS + \mathcal{GP}_0$  configuration. Figure 21(c) shows this to indeed be the case, where the  $AS + \mathcal{GP}_{DL}$  required an offset to locate improved recommendations.

The largest advancement was produced by the  $DL + \mathcal{GP}_0$  configuration at 96.85% with a final objective value of 0.625; furthermore, this achievement was located within just 3 iterations. The addition of the  $\mathcal{GP}_{DL}$  netted a similar reduction but accelerated the discovery to within the first iteration. Table 2 provides summary findings.

Reduction Technique	Minimum Objective Value Found	Found by BO at Iteration Number	Improvement over Initial Solution
Initial	19.802	-	-
Original (5-D) + 0 - GP	19.802	20	0.00%
Active Subspaces (2-D) + 0 - GP	10.86	10	45.15%
Deep Learning Network (3-D) + 0 - GP	0.625	4	96.85%
Original (5-D) + DL - GP	19.427	12	1.89%
Active Subspaces (2-D) + DL - GP	7.07	13	64.32%
Deep Learning Network (3-D) + DL - GP	0.75	1	96.21%

Table 2: Comparison by configuration of their best solutions found during a maximum of 20 BO iterations. Each iteration produced 2 recommendations for evaluation.

### 4.3 Predictions

In this section, we review the improvements made to the simulation outputs as a result of the calibration process. We treat the best of the initial 16 LHS samples as a baseline to compare with the  $DL + \mathcal{GP}_0$  solution.

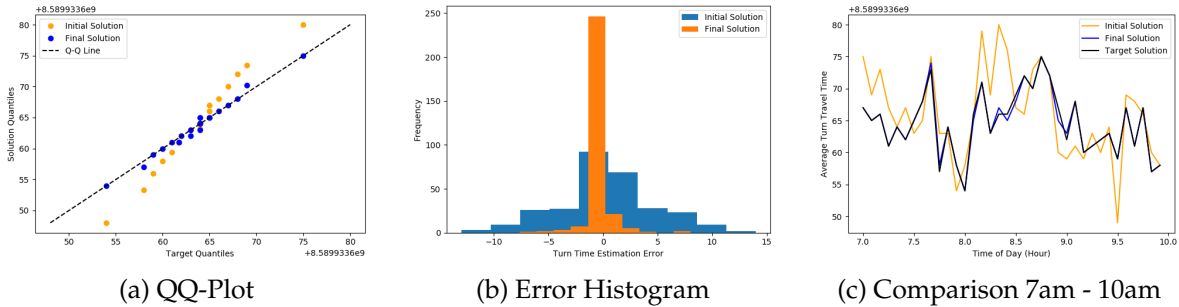


Figure 23: Comparison of the targeted outputs with the initial solution found during the 16 initial sample set and the final solution found by  $DL + \mathcal{GP}_0$  during the 20 iterations of BO. (a) compares each solution’s Quantiles to the targeted solution’s Quantiles. The black, dashed line indicates where the ideal solution should lie. (b) captures the distribution of output errors between the solutions and the targeted solution. (c) shows the average turn times around and at rush hour (7 am - 10 pm)

Figure 23(a) takes a non-parametric approach to compare the solutions in respect to the targeted outputs via a Quantile-Quantile (Q-Q) plot. The plot shows the initial solution aligning in the central quantiles but curving off on either side while the calibrated solution remains in consistent alignment. This indicates that the initial solution was heavy-tailed, or possessed more extreme values than the true solution, and that the calibration process was able to correct the behavior. Figure 23(b) further highlights this accomplishment. The calibrated solution is shown to not only improve the frequency of correct outputs but tighten the initial solution’s extreme deviations.

## 5 Discussion

We provided a Bayesian optimization framework for complex transportation simulators. We have shown that Bayesian optimization algorithms, when combined with dimensionality reduction techniques, provide a good default option for the calibration of transportation ABMs. The Bayesian approach provides several advantages over other black-box optimization techniques: First, the conditional distribution over the

output, provides an efficient approach to maximizing a limited sampling budget (sequential design of computational experiment). Second, the posterior distribution allows for sensitivity analysis and uncertainty quantification to be performed. Although Bayesian optimization has been proposed before for simulation-based problems, our approach, which combines it with dimensionality reduction techniques, allows for solving real-life high-dimensional problems. Our parallel batching strategy and high performance computing framework allow for these approaches to be used by both researchers and transportation practitioners. Future research should consider ‘opening the box’ and shifting the algorithm from recommending future samples based on an aggregated loss function, which averages out the variance across time, to the potential improvements by individual time periods. The model could potentially identify the most important contributors to the acquisition function in this manner and encourage the algorithm to direct its attention to those areas for concentrated improvement.

## A Active Subspaces

Active Subspaces (AS) identifies a linear transformation of the subspace by constructing a set of uncorrelated eigenvectors, known as Principal Components (PCs), defining the “active” subspace. These orthogonal directions, denoted as  $W$ , capture the average variability of the  $\theta$ -to- $\mathcal{L}$  relationship via a differential function  $\mathcal{L} \approx f(\theta) : \mathbb{R}^d \rightarrow \mathbb{R}$ :

$$\max_{\|W\|=1} \mathbb{E} [\|\mathcal{L}(\theta W)\|_0] \quad (29)$$

$$\mathbb{E} [W^T \theta^T \mathcal{L}^T \mathcal{L} \theta W] \quad (30)$$

$$W^T \mathbb{E} [\text{cov}^2(\theta V, \text{mathcal{L}})] W \quad (31)$$

$$W^T C W \quad (32)$$

Given a bounded probability density function  $\rho(\theta) \in \mathbb{R}^d$  on  $f(\theta)$ , AS first decomposes the eigenvalue-eigenvector representation on the gradient  $\nabla_\theta$ :

$$C = \int (\nabla_\theta f)(\nabla_\theta f)^T \rho(\theta) d\theta = \mathcal{W} \Lambda \mathcal{W}^T \quad (33)$$

where  $C$  is a sum of semi-positive definite rank-one matrices,  $\mathcal{W}$  is the matrix of eigenvectors, and  $\Lambda$  is the diagonal matrix of eigenvalues in decreasing order.

In cases where the gradient is unknown, as with most simulations,  $C$  can instead be approximated using an observed set of  $n$  inputs sampled from  $\rho(\theta)$  via Monte Carlo:

$$\hat{C} = \frac{1}{n} \sum_{i=1}^n (\hat{\nabla}_\theta f_i)(\hat{\nabla}_\theta f_i)^T = \hat{\mathcal{W}} \hat{\Lambda} \hat{\mathcal{W}}^T \quad (34)$$

where  $\hat{\nabla}_\theta$  is the observed gradient or an estimated gradient, such as a local or global linear regression models:

$$\begin{aligned} f_i &\approx \hat{\beta}_0 + \hat{\beta}^T \theta_i \\ \nabla_\theta f_i &= \hat{\beta} \end{aligned} \quad (35)$$

Once determined, the PCs are plotted on a log-scale and a dramatic drop in the eigenvalue space, documented as a *gap*, is sought<sup>1</sup>:

<sup>1</sup>if no gap can be found, compiling larger sets of eigenvalues or sampling more within the current eigenvalue framework to increase the eigenvalue accuracy is suggested

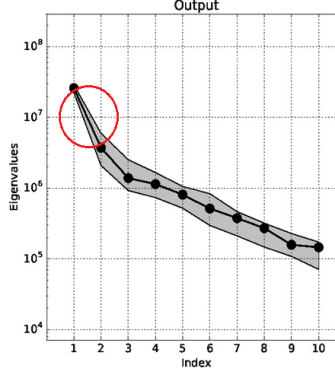


Figure 24: The largest eigenvalue gap is designated by a red circle

The dimensions  $q < d$  to the left of the largest eigenvalue gap is designated the "active" subspace  $v = \hat{\mathcal{W}}_1^T \theta$ ; the remaining  $d - n$  directions define the "inactive" subspace  $z = \hat{\mathcal{W}}_2^T \theta$ .

$$\theta = \hat{\mathcal{W}} \hat{\mathcal{W}}^T \theta = \hat{\mathcal{W}}_1 v + \hat{\mathcal{W}}_2 z \quad (36)$$

The variables of  $z$  are then fixed at nominal values and the active set  $\hat{\mathcal{W}}_1$  subsequently becomes the approximate representation of  $\Theta$ :

$$\begin{aligned} f(\theta) &\approx \int f(\hat{\mathcal{W}}_1 v + \hat{\mathcal{W}}_2 z) p(v | z) dv \\ &\approx g(v) = g(\hat{\mathcal{W}}_1^T \Theta) \end{aligned} \quad (37)$$

For more information behind the derivation of this procedure and its variations, see [24].

Like PCA, AS will require a subsequent, separate regression from the subspace to the output variables  $v \rightarrow f(\theta)$ :

$$f(\theta) = \beta \theta + \epsilon \quad (38)$$

$$\approx \beta v + \epsilon \equiv \beta \hat{\mathcal{W}}_1^T \theta + \epsilon \quad (39)$$

Active Subspaces will provide results closer in line with Partial Least Squares (PLS). This is because, through leveraging the derivatives, the method actively prioritizes those directions which are also relevant to the input-output relationship ultimately being sought. However, the inversion of the lower-dimensional subspace to recover the original variables is complicated by the inactive subspace. For situations in which the inactive eigenvalues are exactly zero,  $f(\theta)$  can be reconstructed without regard to the inactive subspace by setting  $z = 0$ :

$$f(\theta) \approx f(\hat{\mathcal{W}}_1 v) = f(\hat{\mathcal{W}}_1 \hat{\mathcal{W}}_1^T \theta) \quad (40)$$

When the inactive eigenvalues are small but not zero, decoding should be constructed by optimizing over the inactive subspace  $v$  such that:

$$\underset{v \in V}{\text{minimize}} \left[ \begin{array}{l} \underset{z \in Z}{\text{minimum}} \quad f(\hat{\mathcal{W}}_1 v + \hat{\mathcal{W}}_2 z) \\ \text{s.t.} \quad \Theta_{lb} - \hat{\mathcal{W}}_1 v \leq \hat{\mathcal{W}}_2 z \leq \Theta_{ub} - \hat{\mathcal{W}}_1 v \end{array} \right] \quad (41)$$

where  $\Theta_{lb}$  and  $\Theta_{ub}$  are the lower and upper bounds of the original  $\Theta$  state-space, respectively.

## References

- [1] Petter Abrahamsen. Gaussian random fields and correlation functions. Technical report, Technical report, Norwegian Computing Center, Oslo, Norway, 1997.
- [2] Kofi P. Adragani and R. Dennis Cook. Sufficient dimension reduction and prediction in regression. *Philosophical Transactions of the Royal Society A: Mathematical, Physical and Engineering Sciences*, 367(1906):4385–4405, November 2009.
- [3] Joshua Auld, Michael Hope, Hubert Ley, Vadim Sokolov, Bo Xu, and Kuilin Zhang. POLARIS: Agent-based modeling framework development and implementation for integrated travel demand and network and operations simulations. *Transportation Research Part C: Emerging Technologies*, 64:101–116, 2016.
- [4] Joshua Auld, Taha Hossein Rashidi, Mahmoud Javanmardi, and Abolfazl (Kouros) Mohammadian. Dynamic Activity Generation Model Using Competing Hazard Formulation. *Transportation Research Record*, January 2011. Publisher: SAGE PublicationsSage CA: Los Angeles, CA.
- [5] Javad Azimi, Alan Fern, Xiaoli Z Fern, Glencora Borradaile, and Brent Heeringa. Batch Active Learning via Coordinated Matching. page 8, 2012.
- [6] Dmitry Babichev and Francis Bach. Slice inverse regression with score functions. *Electronic Journal of Statistics*, 12(1):1507–1543, 2018.
- [7] Ramachandran Balakrishna, Moshe Ben-Akiva, and Haris N. Koutsopoulos. Offline Calibration of Dynamic Traffic Assignment: Simultaneous Demand-and-Supply Estimation, July 2003.
- [8] Simone Baldi, Iakovos Michailidis, Vasiliki Ntampasi, Elias Kosmatopoulos, Ioannis Papamichail, and Markos Papageorgiou. A Simulation-Based Traffic Signal Control for Congested Urban Traffic Networks. *Transportation Science*, 53(1):6–20, February 2019.
- [9] Andrew R. Barron. Approximation and estimation bounds for artificial neural networks. *Machine Learning*, 14(1):115–133, January 1994.
- [10] R. A. Bates, R. J. Buck, E. Riccomagno, and H. P. Wynn. Experimental Design and Observation for Large Systems. *Journal of the Royal Statistical Society: Series B (Methodological)*, 58(1):77–94, January 1996.
- [11] Moshe E. Ben-Akiva, Steven R. Lerman, and Steven R. Lerman. *Discrete Choice Analysis: Theory and Application to Travel Demand*. MIT Press, 1985. Google-Books-ID: oLC6ZYPs9UoC.
- [12] M. Binois, D. Ginsbourger, and O. Roustant. Quantifying uncertainty on Pareto fronts with Gaussian process conditional simulations. *European Journal of Operational Research*, 243(2):386–394, June 2015.
- [13] Mickael Binois, Robert B. Gramacy, and Michael Ludkovski. Practical heteroskedastic Gaussian process modeling for large simulation experiments. *Journal of Computational and Graphical Statistics*, 27(4):808–821, October 2018. arXiv: 1611.05902.
- [14] Andrew J Booker, JE Dennis, Paul D Frank, Virginia Torczon, and others. A Rigorous Framework for Optimization of Expensive Functions by Surrogates. 1998.
- [15] Eric Brochu, Vlad M. Cora, and Nando De Freitas. A tutorial on Bayesian optimization of expensive cost functions, with application to active user modeling and hierarchical reinforcement learning. *arXiv preprint arXiv:1012.2599*, 2010.
- [16] Tyson Browning. Applying The Design Structure Matrix To System Decomposition And Integration Problems: A Review And New Directions. *Engineering Management, IEEE Transactions on*, 48:292–306, September 2001.

- [17] Francesca Campolongo, Jessica Cariboni, and Andrea Saltelli. An effective screening design for sensitivity analysis of large models. *Environmental modelling & software*, 22(10):1509–1518, 2007.
- [18] Ennio Cascetta and Sang Nguyen. A unified framework for estimating or updating origin/destination matrices from traffic counts. *Transportation Research Part B: Methodological*, 22(6):437–455, 1988.
- [19] Kathryn Chaloner and Isabella Verdinelli. Bayesian experimental design: A review. *Statistical Science*, pages 273–304, 1995.
- [20] Xi Chen, Matteo Diez, Manivannan Kandasamy, Zhiguo Zhang, Emilio F. Campana, and Frederick Stern. High-fidelity global optimization of shape design by dimensionality reduction, metamodels and deterministic particle swarm. *Engineering Optimization*, 47(4):473–494, April 2015.
- [21] R.L. Cheu, X. Jin, K.C. Ng, Y.L. Ng, and D. Srinivasan. Calibration of FRESIM for Singapore expressway using genetic algorithm. *Journal of Transportation Engineering*, 124(6):526–535, November 1998.
- [22] Linsen Chong and Carolina Osorio. A Simulation-Based Optimization Algorithm for Dynamic Large-Scale Urban Transportation Problems. *Transportation Science*, 52(3):637–656, July 2017. Publisher: INFORMS.
- [23] Ernesto Cipriani, Michael Florian, Michael Mahut, and Marialisa Nigro. A gradient approximation approach for adjusting temporal origin–destination matrices. *Transportation Research Part C: Emerging Technologies*, 19(2):270–282, April 2011.
- [24] Paul G. Constantine. *Active Subspaces: Emerging Ideas for Dimension Reduction in Parameter Studies*. Society for Industrial and Applied Mathematics, 2015.
- [25] Emile Contal, David Buffoni, Alexandre Robicquet, and Nicolas Vayatis. Parallel Gaussian Process Optimization with Upper Confidence Bound and Pure Exploration. In David Hutchison, Takeo Kanade, Josef Kittler, Jon M. Kleinberg, Friedemann Mattern, John C. Mitchell, Moni Naor, Oscar Nierstrasz, C. Pandu Rangan, Bernhard Steffen, Madhu Sudan, Demetri Terzopoulos, Doug Tygar, Moshe Y. Vardi, Gerhard Weikum, Camille Salinesi, Moira C. Norrie, and Oscar Pastor, editors, *Advanced Information Systems Engineering*, volume 7908, pages 225–240. Springer Berlin Heidelberg, Berlin, Heidelberg, 2013.
- [26] Corinna Cortes, Patrick Haffner, and Mehryar Mohri. Rational kernels: Theory and algorithms. *Journal of Machine Learning Research*, 5(Aug):1035–1062, 2004.
- [27] G Cybenko. Approximation by superpositions of a sigmoidal function. *Mathematics of Control, Signals, and Systems*, pages 202–214, 1989.
- [28] C. Danielski, T. Kacprzak, G. Tinetti, and P. Jagoda. Gaussian Process for star and planet characterization. *arXiv:1304.6673 [astro-ph]*, April 2013.
- [29] Thomas Desautels, Andreas Krause, and Joel W Burdick. Parallelizing Exploration-Exploitation Tradeoffs in Gaussian Process Bandit Optimization. page 51, December 2014.
- [30] Tamara Djukic, Gunnar Fløtterød, Hans Van Lint, and Serge Hoogendoorn. Efficient real time OD matrix estimation based on Principal Component Analysis. In *Intelligent Transportation Systems (ITSC), 2012 15th International IEEE Conference on*, pages 115–121. IEEE, 2012.
- [31] David L. Donoho. High-dimensional data analysis: The curses and blessings of dimensionality. In *Ams Conference on Math Challenges of the 21st Century*, 2000.
- [32] Nicolas Durrande, David Ginsbourger, Olivier Roustant, and Laurent Carraro. Additive covariance kernels for high-dimensional Gaussian process modeling, 2012.
- [33] David Duvenaud. *Automatic model construction with Gaussian processes*. PhD thesis, University of Cambridge, 2014.

- [34] Michael Florian, Michael Mahut, and Nicolas Tremblay. A hybrid optimization-mesoscopic simulation dynamic traffic assignment model. In *ITSC 2001. 2001 IEEE Intelligent Transportation Systems. Proceedings (Cat. No. 01TH8585)*, pages 118–121. IEEE, 2001.
- [35] Gunnar Flötteröd, Michel Bierlaire, and Kai Nagel. Bayesian Demand Calibration for Dynamic Traffic Simulations. *Transportation Science*, 45(4):541–561, November 2011.
- [36] Gunnar Flötteröd. A general methodology and a free software for the calibration of DTA models. In *The Third International Symposium on Dynamic Traffic Assignment*, 2010.
- [37] A. Forrester, A. Sobester, and A. Keane. *Engineering Design via Surrogate Modelling: A Practical Guide*. 2008.
- [38] Peter I. Frazier. Bayesian Optimization. In *Recent Advances in Optimization and Modeling of Contemporary Problems*, INFORMS TutORials in Operations Research, pages 255–278. INFORMS, October 2018.
- [39] Ken-Ichi Funahashi. On the approximate realization of continuous mappings by neural networks. *Neural Networks*, 2(3):183–192, January 1989.
- [40] Alfredo Garcia, Stephen D. Patek, and Kaushik Sinha. A Decentralized Approach to Discrete Optimization via Simulation: Application to Network Flow. *Operations Research*, 55(4):717–732, August 2007.
- [41] Andrew T. Glaws, Paul G. Constantine, and R. Dennis Cook. Inverse regression for ridge recovery: A data-driven approach for parameter reduction in computer experiments. *arXiv:1702.02227 [math]*, February 2017. arXiv: 1702.02227.
- [42] Robert B. Gramacy and Herbert K. H. Lee. Adaptive Design and Analysis of Supercomputer Experiments. *Technometrics*, 51(2):130–145, May 2009.
- [43] Robert B Gramacy and Herbert KH Lee. Cases for the nugget in modeling computer experiments. *Statistics and Computing*, 22(3):713–722, 2012.
- [44] Robert B. Gramacy and Nicholas G. Polson. Particle Learning of Gaussian Process Models for Sequential Design and Optimization. *Journal of Computational and Graphical Statistics*, 20(1):102–118, January 2011.
- [45] David K. Hale, Constantinos Antoniou, Mark Brackstone, Dimitra Michalaka, Ana T. Moreno, and Kavita Parikh. Optimization-based assisted calibration of traffic simulation models. *Transportation Research Part C: Emerging Technologies*, 55:100–115, June 2015.
- [46] Martin L. Hazelton. Statistical inference for time varying origin - destination matrices. *Transportation Research Part B: Methodological*, 42(6):542–552, July 2008.
- [47] J. C. Helton and F. J. Davis. Latin hypercube sampling and the propagation of uncertainty in analyses of complex systems. *Reliab. Eng. Syst. Saf.*, 2003.
- [48] Dave Higdon, James Gattiker, Brian Williams, and Maria Rightley. Computer Model Calibration Using High-Dimensional Output. *Journal of the American Statistical Association*, 103(482):570–583, June 2008.
- [49] Geoffrey E Hinton and Ruslan R Salakhutdinov. Using Deep Belief Nets to Learn Covariance Kernels for Gaussian Processes. In J. C. Platt, D. Koller, Y. Singer, and S. T. Roweis, editors, *Advances in Neural Information Processing Systems 20*, pages 1249–1256. Curran Associates, Inc., 2008.
- [50] Kurt Hornik. Approximation capabilities of multilayer feedforward networks. *Neural Networks*, 4(2):251–257, January 1991.
- [51] Donald R. Jones, Matthias Schonlau, and William J. Welch. Efficient global optimization of expensive black-box functions. *Journal of Global optimization*, 13(4):455–492, 1998.

- [52] Kirthevasan Kandasamy, Jeff Schneider, and Barnabás Póczos. Bayesian Active Learning for Posterior Estimation. In *Proceedings of the 24th International Conference on Artificial Intelligence, IJCAI'15*, pages 3605–3611. AAAI Press, 2015. event-place: Buenos Aires, Argentina.
- [53] Marc C. Kennedy and Anthony O'Hagan. Bayesian calibration of computer models. *Journal of the Royal Statistical Society: Series B (Statistical Methodology)*, 63(3):425–464, January 2001.
- [54] Patrick Koch, Timothy Simpson, Janet Allen, and Farrokh Mistree. Statistical Approximations for Multidisciplinary Design Optimization: The Problem of Size. *Journal of Aircraft*, 36:275–286, January 1999.
- [55] A. N. Kolmogorov. On the Approximation of Distributions of Sums of Independent Summands by Infinitely Divisible Distributions. *Sankhyā: The Indian Journal of Statistics, Series A (1961-2002)*, 25(2):159–174, 1963. Publisher: Springer.
- [56] Neil D. Lawrence. Gaussian process latent variable models for visualisation of high dimensional data. In *Advances in neural information processing systems*, pages 329–336, 2004.
- [57] Jung Beom Lee and Kaan Ozbay. New calibration methodology for microscopic traffic simulation using enhanced simultaneous perturbation stochastic approximation approach. *Transportation Research Record*, (2124):233–240, 2009.
- [58] M. J. Lighthill and G. B. Whitham. On kinematic waves II. A theory of traffic flow on long crowded roads. *Proceedings of the Royal Society of London. Series A. Mathematical and Physical Sciences*, 229(1178):317–345, May 1955.
- [59] Xiaoyu Liu and Serge Guillas. Dimension Reduction for Gaussian Process Emulation: An Application to the Influence of Bathymetry on Tsunami Heights. *SIAM/ASA Journal on Uncertainty Quantification*, 5(1):787–812, January 2017.
- [60] Chung-Cheng Lu, Xuesong Zhou, and Kuilin Zhang. Dynamic origin–destination demand flow estimation under congested traffic conditions. *Transportation Research Part C: Emerging Technologies*, 34:16–37, September 2013.
- [61] Lu Lu, Yan Xu, Constantinos Antoniou, and Moshe Ben-Akiva. An enhanced SPSA algorithm for the calibration of Dynamic Traffic Assignment models. *Transportation Research Part C: Emerging Technologies*, 51:149–166, February 2015.
- [62] T. Ma and B. Abdulhai. Genetic algorithm-based optimization approach and generic tool for calibrating traffic microscopic simulation parameters. *Intelligent Transportation Systems and Vehicle-highway Automation 2002: Highway Operations, Capacity, and Traffic Control*, (1800):6–15, 2002.
- [63] Xingjun Ma, Yisen Wang, Michael E. Houle, Shuo Zhou, Sarah M. Erfani, Shu-Tao Xia, Sudanthi Wijewickrema, and James Bailey. Dimensionality-Driven Learning with Noisy Labels. *arXiv:1806.02612 [cs, stat]*, June 2018. arXiv: 1806.02612.
- [64] Amandine Marrel, Bertrand Iooss, Michel Jullien, Béatrice Laurent, and Elena Volkova. Global sensitivity analysis for models with spatially dependent outputs. *Environmetrics*, 22(3):383–397, May 2011.
- [65] M. D. McKay, R. J. Beckman, and W. J. Conover. A Comparison of Three Methods for Selecting Values of Input Variables in the Analysis of Output from a Computer Code. *Technometrics*, 21(2):239–245, 1979. Publisher: [Taylor & Francis, Ltd., American Statistical Association, American Society for Quality].
- [66] M. Mesbah, M. Sarvi, and G. Currie. Optimization of Transit Priority in the Transportation Network Using a Genetic Algorithm. *IEEE Transactions on Intelligent Transportation Systems*, 12(3):908–919, September 2011.

- [67] Mahmoud Mesbah, Majid Sarvi, Iradj Ouveysi, and Graham Currie. Optimization of transit priority in the transportation network using a decomposition methodology. *Transportation Research Part C: Emerging Technologies*, 19(2):363 – 373, 2011.
- [68] N Michelena and Panos Papalambros. Optimal Model-Based Partitioning of Powertrain System Design. June 2019.
- [69] Jonas Mockus. *Bayesian Approach to Global Optimization: Theory and Applications*. Springer Science & Business Media, December 2012. Google-Books-ID: VuKoCAAQBAJ.
- [70] Jorge J Moré and Stefan M Wild. Benchmarking derivative-free optimization algorithms. *SIAM Journal on Optimization*, 20(1):172–191, 2009. Publisher: SIAM.
- [71] Thomas Muehlenstaedt. Data-driven Kriging models based on FANOVA-decomposition, 2012.
- [72] Kai Nagel and Gunnar Flötteröd. Agent-based traffic assignment: Going from trips to behavioural travelers. In *Travel Behaviour Research in an Evolving World—Selected papers from the 12th international conference on travel behaviour research*, pages 261–294. International Association for Travel Behaviour Research, 2012.
- [73] Prasad A Naik and Chih-Ling Tsai. Constrained Inverse Regression for Incorporating Prior Information. *Journal of the American Statistical Association*, 100(469):204–211, March 2005.
- [74] G. F. Newell. A simplified theory of kinematic waves in highway traffic, part II: Queueing at freeway bottlenecks. *Transportation Research Part B: Methodological*, 27(4):289–303, August 1993.
- [75] Carolina Osorio and Krishna Kumar Selvam. Simulation-based optimization: achieving computational efficiency through the use of multiple simulators. *Transportation Science*, 51(2):395–411, 2017.
- [76] Nicholas G Polson and Vadim O Sokolov. Deep learning for short-term traffic flow prediction. *Transportation Research Part C: Emerging Technologies*, 79:1–17, 2017.
- [77] Carl Edward Rasmussen and Christopher K. I. Williams. *Gaussian processes for machine learning*. Adaptive computation and machine learning. MIT Press, Cambridge, Mass, 2006. OCLC: ocm61285753.
- [78] Paul I. Richards. Shock Waves on the Highway. *Operations Research*, February 1956.
- [79] Philip A. Romero, Andreas Krause, and Frances H. Arnold. Navigating the protein fitness landscape with Gaussian processes. *Proceedings of the National Academy of Sciences*, 110(3):E193–E201, 2013.
- [80] Roman Rosipal. Kernel Partial Least Squares for Nonlinear Regression and Discrimination. *Neural Network World*, (3):11, 2003.
- [81] Elizabeth G. Ryan. *Contributions to Bayesian experimental design*. PhD thesis, Queensland University of Technology, 2014.
- [82] Jerome Sacks, William J. Welch, Toby J. Mitchell, and Henry P Wynn. Design and Analysis of Computer Experiments. *Statistical Science*, 4(4):409–423, November 1989.
- [83] Karim Saheb Etabaa and Manel Ben Salem. Adaptive Progressive Band Selection for Dimensionality Reduction in Hyperspectral Images. *Journal of the Indian Society of Remote Sensing*, 46(2):157–167, February 2018.
- [84] Andrea Saltelli, Stefano Tarantola, Francesca Campolongo, and Marco Ratto. *Sensitivity analysis in practice: a guide to assessing scientific models*, volume 1. Wiley Online Library, 2004.
- [85] Alexandra M Schmidt, Kelly CM Gonçalves, and Patrícia L Velozo. Spatiotemporal models for skewed processes. *Environmetrics*, 28(6):e2411, 2017. Publisher: Wiley Online Library.
- [86] Alexandra M. Schmidt, Peter Guttorp, and Anthony O’Hagan. Considering covariates in the covariance structure of spatial processes. *Environmetrics*, 22(4):487–500, June 2011.

- [87] Laura Schultz and Vadim Sokolov. Bayesian Optimization for Transportation Simulators. *Procedia Computer Science*, 130:973–978, 2018.
- [88] Di Sha, Kaan Ozbay, and Yue Ding. Applying bayesian optimization for calibration of transportation simulation models. *Transportation Research Record*, 2674(10):215–228, 2020.
- [89] Amar Shah and Zoubin Ghahramani. Parallel Predictive Entropy Search for Batch Global Optimization of Expensive Objective Functions. *arXiv:1511.07130 [cs, stat]*, November 2015. arXiv: 1511.07130.
- [90] Songqing Shan and G Gary Wang. Survey of modeling and optimization strategies to solve high-dimensional design problems with computationally-expensive black-box functions. *Structural and Multidisciplinary Optimization*, 41(2):219–241, 2010.
- [91] Songqing Shan and G. Gary Wang. Survey of modeling and optimization strategies to solve high-dimensional design problems with computationally-expensive black-box functions. *Structural and Multidisciplinary Optimization*, 41(2):219–241, March 2010.
- [92] Jeffrey A. Shorter, Precila C. Ip, and Herschel A. Rabitz. An Efficient Chemical Kinetics Solver Using High Dimensional Model Representation. *The Journal of Physical Chemistry A*, 103(36):7192–7198, September 1999.
- [93] Jasper Snoek, Hugo Larochelle, and Ryan P. Adams. Practical bayesian optimization of machine learning algorithms. In *Advances in neural information processing systems*, pages 2951–2959, 2012.
- [94] Jasper Snoek, Oren Rippel, Kevin Swersky, Ryan Kiros, Nadathur Satish, Narayanan Sundaram, Mostofa Patwary, Mr Prabhat, and Ryan Adams. Scalable bayesian optimization using deep neural networks. In *International conference on machine learning*, pages 2171–2180, 2015.
- [95] Jasper Snoek, Kevin Swersky, Richard S. Zemel, and Ryan P. Adams. Input Warping for Bayesian Optimization of Non-Stationary Functions. In *ICML*, pages 1674–1682, 2014.
- [96] A Srivastava, K Hacker, Kemper Lewis, and Timothy Simpson. A method for using legacy data for metamodel-based design of large-scale systems. *Structural and Multidisciplinary Optimization*, 28:146–155, September 2004.
- [97] Jelka Stevanovic, Aleksandar Stevanovic, Peter T. Martin, and Thomas Bauer. Stochastic optimization of traffic control and transit priority settings in VISSIM. *Transportation Research Part C: Emerging Technologies*, 16(3):332 – 349, 2008.
- [98] Matthew A. Taddy. Big Data: Factors, January 2018.
- [99] Jian Tu and Donald Jones. Variable Screening in Metamodel Design by Cross-Validated Moving Least Squares Method. April 2003.
- [100] Jialei Wang, Scott C. Clark, Eric Liu, and Peter I. Frazier. Parallel Bayesian Global Optimization of Expensive Functions. *arXiv:1602.05149 [math, stat]*, February 2016. arXiv: 1602.05149.
- [101] Andrew Gordon Wilson, Zhiting Hu, Ruslan Salakhutdinov, and Eric P Xing. Deep kernel learning. In *Artificial Intelligence and Statistics*, pages 370–378, 2016.
- [102] Jian Wu and Peter I. Frazier. The Parallel Knowledge Gradient Method for Batch Bayesian Optimization. *arXiv:1606.04414 [cs, stat]*, June 2016. arXiv: 1606.04414.
- [103] Jing Xie, Peter I. Frazier, and Stephen E. Chick. Bayesian Optimization via Simulation with Pairwise Sampling and Correlated Prior Beliefs. *Operations Research*, 64(2):542–559, April 2016.
- [104] Miao Yu and Wei (David) Fan. Calibration of microscopic traffic simulation models using metaheuristic algorithms. *International Journal of Transportation Science and Technology*, 6(1):63–77, June 2017.
- [105] Chao Zhang, Carolina Osorio, and Gunnar Flötteröd. Efficient calibration techniques for large-scale traffic simulators. *Transportation Research Part B: Methodological*, 97:214–239, March 2017.

- [106] Zhang Lei, Chang Gang-Len, Zhu Shanjiang, Xiong Chenfeng, Du Longyuan, Mollanejad Mostafa, Hopper Nathan, and Mahapatra Subrat. Integrating an Agent-Based Travel Behavior Model with Large-Scale Microscopic Traffic Simulation for Corridor-Level and Subarea Transportation Operations and Planning Applications. *Journal of Urban Planning and Development*, 139(2):94–103, June 2013.
- [107] Xuesong Zhou. DYNAMIC ORIGIN-DESTINATION DEMAND ESTIMATION AND PREDICTION FOR OFF-LINE AND ON-LINE DYNAMIC TRAFFIC ASSIGNMENT OPERATION. August 2004. Accepted: 2004-08-27T05:36:30Z.
- [108] Xuesong Zhou and Hani S. Mahmassani. A structural state space model for real-time traffic origin–destination demand estimation and prediction in a day-to-day learning framework. *Transportation Research Part B: Methodological*, 41(8):823–840, October 2007.
- [109] Zheng Zhu, Chenfeng Xiong, Xiqun (Michael) Chen, and Lei Zhang. Calibrating supply parameters of large-scale DTA models with surrogate-based optimisation. *IET Intelligent Transport Systems*, April 2018.
- [110] Byungkyu “Brian” Park, Ilsoo Yun, and Kyoungho Ahn. Stochastic optimization for sustainable traffic signal control. *International journal of sustainable transportation*, 3(4):263–284, 2009. Publisher: Taylor & Francis.